

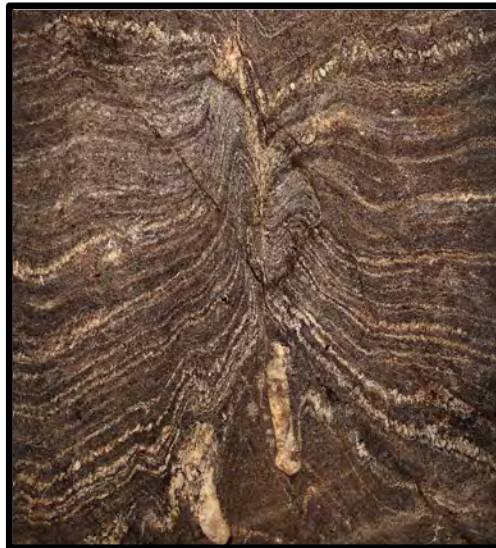
MACQUARIE UNIVERSITY

**Migmatite delineates zones of melt flux through
the upper crust, Wongwibinda, NSW**

Michael Farmer

Masters of Research Thesis

Submission date: 09/10/2017



Department of Earth & Planetary Sciences in
The Faculty of Science and Engineering,
Macquarie University, North Ryde,
Australia



MACQUARIE
University
SYDNEY · AUSTRALIA

Statement of originality:

I certify that, to the best of my knowledge, the work presented herein is the original work of the author and has not been presented or published elsewhere. All published works and work carried out by persons other than the author presented here are appropriately referenced and due respect given to the participants. Further no part of this thesis has been presented, accepted or been published for the award or consideration of a higher degree or diploma at this or any other educational institution.

Signed:**Michael James Farmer**

09/10/2017

Acknowledgements

I have had a great time over the last nine months getting this thesis ready for submission. The places I have been fortunate enough to travel to and experience I've gained has benefited me greatly. This aside, it takes more than just one person to complete a project of this scale and as such, there are several people I would like to thank.

Firstly, my two supervisors Nathan Daczko and Sandra Piazzolo. Nathan, for sticking with me and being there throughout the thesis, door always open, last minute meetings/revisions rarely turned down. I admire your incredible knowledge of metamorphic and structural geology, your big picture visualisation and most of all, your passion. Sandra, for her incredible generosity in supporting my trip over to Leeds to work with her at the University, despite still being in the process of moving a whole house and family across the globe. Your assistance, expert knowledge, passion for EBSD, quick revisions and pre-6am Skype meetings were very much appreciated. It has been a pleasure working with both of you and I wish the best for you and your families.

Kim Jessop for your encyclopedic knowledge of just about every word that has ever been said about the WMC and your ongoing support during the year. The wealth of data you have provided for the project (maps, analyses, samples and insight) has not only benefited the research, but also helped me get through. Thanks also to Rod for chauffeuring to Armidale and then through the field, chasing cows off the outcrops and providing food and hot beverages on site – the most luxurious fieldwork I've ever done. Thank you.

Angela Mabee for being a better field work companion than anyone could hope for. The information you retained and being able to bounce ideas off you has improved my thinking on the topic. Wandering around Armidale trying to find a printer that worked was also an interesting experience!

Robyn Gardner and Cait Stuart. Your help with the various software I was unfamiliar with and discussions about results has made this a smoother process for me. Thank you.

Peter Wieland, Tim Murphy and Yi-Jen Lai for helping get most of my analyses done. I really do appreciate the early mornings, late nights and putting up with my 'stupid' questions, thank you.

Manal for putting up with the slow trickle of thin sections through the year. Trust me, there are no more now (from me at least).

To my MRes cohort, we did it lads. The comradery and support from you guys has made this year and all the others I've shared with you, a pleasure.

Lastly, but definitely not least, my family, house mates and friends. Without the foundation of support you have provided me, I doubt this would have been possible. Thank you.

Abstract

The small (<20km wide) high-temperature – low-pressure (HTLP) Wongwibinda Metamorphic Complex (WMC), southern New England Orogen, is characterised by an irregular elevated metamorphic field gradient (<100°C/km). An examination of the migmatite rocks shows they did not experienced significant in-situ partial melting, suggesting the abundant leucocratic veins and dykes observed in outcrop are externally derived. Using a combined field and petrographic study, augmented by targeted electron backscatter diffraction (EBSD) and whole-rock geochemical analyses, two types of melt pathways through the migmatite have been identified: (i) veining and dyking, and (ii) grain-scale channelled porous flow. The pathways of porous flow are recognised across the field area as cm- to outcrop-scale channels, characterised by rare-earth element (REE) metasomatism, mineral mode changes, a randomisation of host crystallographic preferred orientation fabrics and the presence of cusped K-feldspar pockets. The identification of collapse structures, due to volume loss as melt-filled dykes and voids drained, demonstrates that some of the injected melt escaped to structurally higher levels. The two types of melt pathways and their characteristics supports a melt flux hypothesis, which is interpreted to drive migmatitisation and promote the formation of the elevated thermal field gradient.

1. Introduction

The Wongwibinda Metamorphic Complex is a small (<20 km wide) high-temperature – low-pressure (HTLP) zone in the southern New England Orogen, located 25km northeast of Armidale, NSW, Australia (Fig. 1). The complex is dominantly fine-grained schists that change from low grade in the west to high-grade amphibolite facies schists in the east (Farrell, 1992; Craven et al., 2012, 2013). These are intruded by the S-type Hillgrove Plutonic Suite, including the Abroi Granodiorite adjacent to an area of migmatite (Fig. 1). This ‘Zone of Migmatites’ has been characterised before, linking its features to the regional metamorphic and deformation history (Farrell, 1992; Danis et al., 2010; Craven et al., 2012, 2013). However, the mechanism facilitating the local steep thermal field gradient has not been fully constrained. Previous interpretations have linked the migmatite rocks and HTLP metamorphism to the intrusive suite due to their close spatial relationship (Binns, 1966; Vernon, 1982). However, recent dating by Craven et al. (2012) suggests that the Abroi Granodiorite (290.5 ± 1.6 Ma) post-dates peak metamorphism (296.8 ± 1.8 Ma). Craven et al. (2013) focused on cordierite-bearing schists in the complex and proposed that heat advection by aqueous fluids, channelled in shear zones, drove local HTLP metamorphism explaining the steep thermal field gradient (up to $\sim 100^\circ\text{C}/\text{km}$, Fig. 1, Craven et al., 2012) in the sub-solidus rocks. However, heat production by hydrothermal fluid flux alone requires very high time integrated fluid fluxes to produce the peak temperatures experienced by the migmatite rocks ($\sim 660^\circ\text{C}$, Craven et al., 2012), suggesting an additional mechanism is required to explain the highest-grade parts of the metamorphic complex. This study supplements the previous work by focusing on the migmatite rocks. It is demonstrated that externally-derived melt fluxed through the ‘Zone of Migmatites’. Fluxing occurs in two main ways: (i) veining and dyking and (ii) channelled porous flow. Based on the evidence of externally derived melt fluxing, it is concluded that a combination of hot fluid fluxing in the non-migmatitic portions of the complex along with melt fluxing in the migmatite zone presents a compelling scenario for the observed high temperature gradient in the Wongwibinda Metamorphic Complex. As such, fluid and melt fluxing may have also caused the high temperature gradients in other high temperature, low pressure complexes.

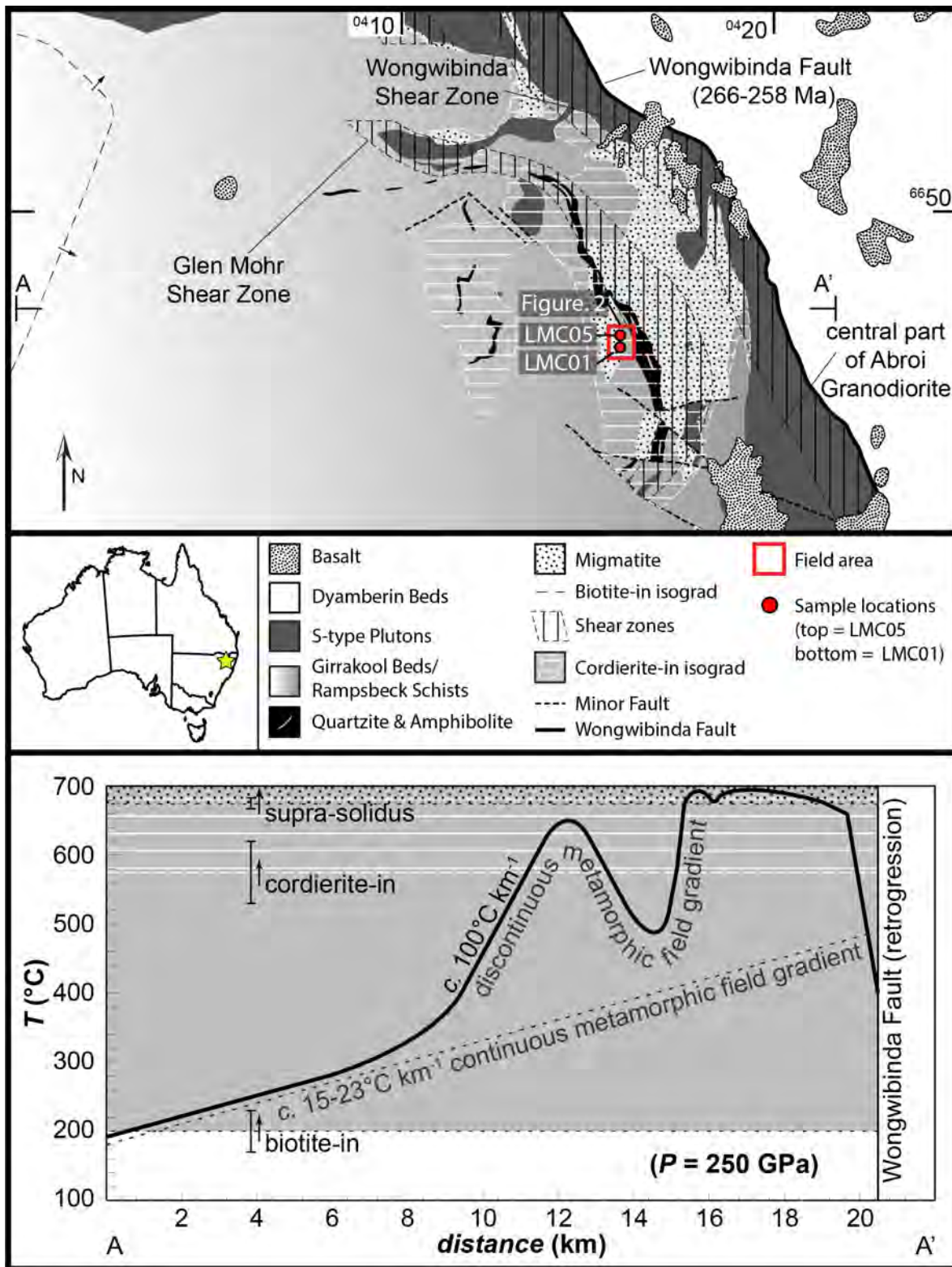


Fig. 1: Top: Wongwibinda Metamorphic Complex (WMC) geological map (modified from Craven et al., 2013). Inset shows location of the WMC in Australia. Red circles = location of two samples in this study (LMC05 & LMC01). Bottom: Calculated thermal field gradient across field transect A-A' (modified from Craven et al., 2013). Note that migmatites in this study are part of the supra-solidus component (i.e. highest temperatures in the complex).

High-temperature-low-pressure metamorphism

High-temperature – low-pressure (HTLP) metamorphism requires an elevated thermal gradient ($>35^{\circ}\text{C}$, Bodorkos et al., 2002) in shallow ($<12\text{km}$) upper crustal rocks. This is usually defined when temperatures exceed 600°C , but pressures remain below 0.5GPa (Sandiford & Hand, 1998). Examples of other HTLP zones elsewhere in the world include: the Cooma Metamorphic Complex in Australia, Variscan Metamorphic Complex in Germany and Hidaka Belt in Japan (Richards & Collins, 2002; Kalt et al., 2000; Kemp et al., 2007). Interpretations regarding the mechanism(s) that form these anomalous conditions vary. Several mechanisms are proposed: (i) crustal thinning by continental extension allowing for the conduction of heat from the lower crust/upper mantle (Bodorkos et al., 2002), (ii) radioactive heat production causing conductive heat transfer to adjacent rocks (Sandiford et al., 1998; Huerta et al., 1998), (iii) advective heat transfer from mantle-derived basaltic magma emplacement, or conductive dissipation from large volumes of intruded granitoids (Lux et al., 1986; Bodorkos et al., 2002), (iv) advective heat transfer due to hydrothermal activity (Craven et al., 2013), (v) drag imposed on a rising diapiric pluton by the host rock (Flood & Vernon, 1978), and (vi) denudation causing crustal thinning (Winslow et al., 1994). While each of the above could be the sole mechanism to produce a HTLP zone, a combination of mechanisms should not be discounted.

Regional geology

The Wongwibinda Metamorphic Complex (WMC) is a 400km^2 HTLP zone of metamorphosed deep marine turbidites in the southern New England Orogen (Fig. 1). The New England Orogen is a deformed fore-arc basin and accretionary wedge pair (Jenkins et al., 2002), consisting of the Tamworth Belt and the more deformed Tablelands Complex (Leitch, 1974; Korsch, 1981); the WMC is part of the latter. The protolith of the WMC is the Devonian-Carboniferous Girrorakool Beds: an accreted, deep marine, medium to fine grained, repetitive turbidite sequence (Korsch, 1977) with rare metabasite, quartzite and calcareous nodules (Craven et al., 2012). These beds were metamorphosed to biotite grade in the west of the WMC, through the Rampsbeck Schists, to peak amphibolite facies ($T\sim 660^{\circ}\text{C}$, $P\sim 0.3\text{GPa}$, Craven et al., 2012) in the east. This transition from low to high grade occurs over $\sim 20\text{km}$ with steep thermal gradients $>100^{\circ}\text{C}/\text{km}$ (Fig. 1, Craven et al., 2012). A zone of migmatite is spatially associated with the amphibolite facies rocks (Farrell, 1992; Danis et al., 2010; Craven et al., 2012, 2013). Adjacent to this are intrusive granitoids of the

Late Carboniferous-Early Permian, S-type Hillgrove Plutonic Suite (Binns, 1966), including the Abroi Granodiorite (Farrell, 1992, Craven et al., 2012). This encompasses the Wongwibinda Metamorphic Complex on its northern, eastern and southern boundaries (Fig. 1). Shear zones (Glen Mohr and Wongwibinda) are present in the higher-grade rocks, migmatites and Abroi Granodiorite (Farrell, 1992; Craven et al., 2012, 2013 - Fig. 1). The Wongwibinda Fault forms a sharp boundary at the complexes eastern edge (Fig. 1). Dating of the Abroi Granodiorite (290.5 ± 1.6 Ma, Craven et al., 2012) places it within error of being coeval with deformation in the Glen Mohr shear zone (291 ± 1.8 Ma, Craven et al., 2013) and younger than peak amphibolite facies metamorphism in migmatite (296.8 ± 1.5 Ma, Craven et al., 2012).

Migmatite: Formation and components

Migmatite rocks are striking, often light–dark foliated rocks, composed of an igneous (often granitic) and metamorphic (often schist or gneiss) component (Brown, 1973; Sayer, 2008). ‘Classic’ migmatite forms due to partial melting (anatexis) and melt segregation where lighter felsic phases are separated leaving a darker residuum (Brown, 1973; Sayer, 2008). Migmatites can also be formed in cooler, near solidus conditions by the pervasive injection of veins and dykes. These areas are called injection complexes and represent an area just above the solidus where melt can move before freezing (Weinberg & Searle, 1998; Morfin et al., 2013).

Migmatite classification is to be treated cautiously and nomenclature used varies widely from author to author. The definitions within Sawyer (2008) are used here. The portion of rock that has undergone partial-melting is termed, the ‘neosome’ (Johannes, 1988; Sawyer, 2008) and is subdivided into light and dark fractions. The lighter fraction is termed ‘leucosome’ representing the fractionated melt, generally more felsic and rich in quartz and K-feldspar (Johannes, 1988; Vernon & Collins, 1988). These light bands are further sub-divided based on the relationship to their source: (i) In-situ: melt remains at the site of melt formation; (ii) In-source: melt migrated from the site of melting, but remained in the source layer; (iii) Leucocratic vein/dyke: melt migrated out of the source layer and injected into another rock, and remained in the area affected by the anatexis event (Sawyer, 2008). The darker fraction, termed ‘residuum’ (also called melanosome or restite in other literature) is more mafic, rich in biotite and represents what is left over after the felsic melt portion has been extracted (White & Chappell, 1977; Sawyer, 1998). Occasionally, a thin, dark rim surrounds the in-situ, in source leucosome or leucocratic vein/dykes, but isn’t residuum (though it is

often misinterpreted or referred to as residuum). These are termed ‘selvages’ (Hughes, 1970; Guernina & Sawyer, 2003) and are generally compositionally, mineralogically and microstructurally different from the leucosome/vein and surrounding host rock (Sawyer, 2008). These are proposed to be a result of one or a combination of the following: (i) reaction between host rock and aqueous fluid exsolved from the leucosome/vein melt (Sawyer, 2008); (ii) reaction of the host rock and the injected melt itself (Sawyer, 2008); (iii) diffusional transfer due to a difference in chemical potential between two components (Sawyer, 2008). These selvages are not unique to migmatites. Migmatites often have a large portion of neosome that cannot be classified as either leucosome or melanosome. This is often referred to as ‘mesosome’. However, this term is used loosely in the literature. The term ‘host’ is used in this study. Finally, rock that hasn’t melted is termed ‘palaeosome’ (Sawyer, 2008) with the portion unaltered during anatexis being called ‘*resisters*’. The light-dark banding in migmatites can record folding and other deformation events during and after (Fleming & White, 1984; Hand & Dirks, 1992; Hasalova et al., 2008) anatexis. However, interpretations are to be treated with caution due to the difficulty in understanding migmatite components.

Structures in Migmatites: Deformation versus melt migration

Interpreting the deformation history of migmatites can be difficult, potentially leading to misinterpretations of regional events. Deviation in the foliation of leucosomes, veins and dykes within the migmatites are used to interpret deformation such as folding, faulting or shearing on a regional scale (Brown, 1973). To correctly identify a regional deformation event, a correct interpretation of the mechanism that formed the structures in the migmatite is necessary.

In contrast to the mentioned structures related to regional deformation events, so called *collapse structures* are interpreted as primary intrusive structures, formed by the ductile collapse of a fluid- or melt-filled void during and after extraction of that fluid/melt (Bons, 1999; Bons et al., 2004). As fluid or melt moves in discreet pockets via ‘stepwise accumulation’ (Bons et al., 2001), the host rock must deform passively to accommodate the inflation as melt injects and deflation as melt escapes in the rocks, as it migrates. This results in a localised deviation in the existing host rock foliation, producing different geometries, influenced by several factors: (i) shape of the fluid- or melt-filled void; (ii) amount of fluid in the void; (iii) direction of wall collapse; (iv) orientation of void and collapse to the existing foliation; (v) external stresses, e.g. shearing (for examples of different collapse geometry, see Bons et al., 2004, 2008, 2009).

An interpretation of collapse structures opposed previously interpreted deformation structures in the Cap de Creus in north-eastern Spain (Bons et al., 2004). The metamorphic host contains elongate pegmatite structures, termed “bead strings”, consisting of captured quartz aggregates connected by a thin “connecting seam.” These were previously interpreted as boudinaged pegmatite veins/dykes, resulting from shearing of the host rock after emplacement (Carreras & Druguet, 1994). Bons et al. (2004) appropriately termed these structures “apparent boudinage” or “pseudo-boudinage” with the quartz aggregates interpreted to be crystallised grains in a fluid/melt that were captured by the collapsing host rock walls as the fluid/melt was expelled – this process occurring independent of external stresses (Bons et al., 2004).

Melt recognition and migration

Recognising the former presence of melt and its interaction with different structures in an outcrop can elucidate a sequence of intrusive events, providing insight into regional stresses and the timing of geological events. While outcrop-scale structures might indicate the presence of melt, analysis at the microscale can yield a suite of useful information. Vernon (2011) provides a set of reliable criteria to determine the former presence of melt in rocks including: (i) quartz+K-feldspar+plagioclase aggregates in veins, (ii) inclusion free euhedral overgrowths of feldspar onto residual grains of feldspar with abundant inclusions, (iii) aligned euhedral feldspar, (iv) simple twinning in K-feldspar, (v) dihedral angles of 60° where quartz or feldspar (inferred to have crystallised) from melt meet two other minerals, (vi) cusped shaped grains of quartz, K-feldspar or sodic plagioclase, (vii) veinlets of inferred former melt, (viii) biotite pseudomorphed by feldspar, (ix) veinlets of plagioclase that are more sodic than adjacent host grains, (x) plagioclase with oscillatory zoning, (xi) microgranophyric intergrowths of quartz and alkali feldspar in patches or veins between primary grains, (xii) symplectic replacement aggregates, (xiii) melanosome patches and layers from which leucosome has been extracted. These microstructural observations can be applied to veins and dykes as well as to a rock that may have been pervasively fluxed at the grain-scale. However, the variability in geological samples and systems means that satisfying only a few of these criteria might be possible in many examples of formerly melt-bearing rocks.

Melt migration from an anatectic source to the emplacement of plutons is highly debated (Brown, 1999; Bons et al., 2001; Brown, 2013), particularly the melt pathways or transport mechanisms (Weinberg & Mark, 2008, Brown, 2013). Melt movement is primarily driven by a negative buoyancy (i.e. the melt is less dense than its surroundings, causing it to rise. (Brown, 2013). Near

the solidus, these processes involve a hotter melt moving through a cooler host and thus heat is lost from the melt resulting in crystallisation and freezing of the melt (Weinberg & Searle, 1998). For the melt to keep moving (flux), several factors have been proposed: (i) increase the temperature or lower the pressure (Langmuir et al., 1993), (ii) add water, lowering the melting temperature (Weinberg & Hasalova, 2015) (iii) undercooling, whereby the melt cools significantly below where it would normally freeze before nucleation occurs (Swanson, 1997). Two dominant melt transport mechanisms have been proposed: (i) veining and dyking by ‘magma-fracture’ and/or (ii) pervasive movement of melt through zones of higher permeability (Weinberg & Searle, 1998; Brown, 2013).

Aims

The aims of this study are to: (i) characterise the migmatite rocks of the high-temperature –low-pressure Wongwibinda Metamorphic Complex, by a combined field, microstructural and whole rock geochemical approach, and (ii) identify the former presence of melt and how it has migrated through the migmatites. This could have implications for the sources of heat and plutons in the complex and broadly, for HTLP complex thermal gradients.

2. Methods

Fieldwork and sample collection

Fieldwork was conducted on Lynoch Station, 56km northeast of Armidale, NSW between 1st-3rd August 2016. The area surveyed is part of the Wongwibinda Metamorphic Complex and provides an excellent exposure of HTLP migmatite rocks. Five outcrops (sites 1-6) were investigated and mapped in detail by marking 10 separate ~1m² grids. These grids were then cleaned with bleach, water and wire brushes to remove heavy lichen and moss cover before 25cm² photos were systematically taken of each site and later stitched together to form high resolution photos of the gridded areas. These were printed in A3 and used with overlays to map in detail. The resulting overlay maps highlight foliations and leucocratic veins and dykes, and digitized version are presented in the field relationships section.

In-situ sample collection was difficult due to the flat nature of the outcrops. Oriented samples were taken, generally outside the detailed maps and one sample (LMC01C) was taken from the corner of detailed map 01B, thus allowing for a more detailed contextual analysis of the visible structures.

Other loose samples were taken from the nearby float with careful consideration of the features observed in the outcrops.

Sample Preparation

Samples were prepared at Macquarie University. 15 samples were mounted to glass slides and polished to ~30microns thick. Two thin sections were duplicated on pure quartz slides for detailed chemical examination at the Australian Synchrotron. A Nikon Eclipse 50iPOL polarizing microscope was used to examine the petrographic characteristics of all samples with four being chosen for EBSD analysis.

Back-scatter Electron (BSE) and Electron Dispersive Spectroscopy (EDS)

Detailed BSE images of microstructures and EDS microchemical data were collected on the Zeiss EVO MA15 Scanning Electron Microscope (SEM) at Macquarie GeoAnalytical, (Macquarie University, Sydney). Samples were coated with ~8-10nm of carbon before analyses were run at high vacuum, 20kV accelerating voltage, beam current of 5-10nA and working distances between 11.5-12.5mm. Stitched BSE and single high-resolution BSE images and EDS data were acquired using the AzTec software from Oxford Instruments. Stitched maps were taken at 45x magnification.

Electron Backscatter Diffraction (EBSD)

EBSD and EDS data was collected simultaneously using the FEI Quanta 650 FEG-ESEM (with Oxford X-max 80 SDD EDS, Oxford/HKL Nordlys S EBSD system and Aztec software) at the Electron Optics Facility, University of Leeds, UK. Samples were polished for an additional 8 minutes with a colloidal silica-water solution to reduce polishing imperfections, then thinly coated with ~3nm of carbon. Analyses were performed with an acceleration voltage of 20kV, working distance of ~12mm and specimen tilt of 70°. Twenty EBSD maps were taken across three samples with step sizes ranging from 2-30µm (step size determined by grain size and required resolution). Data was processed in the Oxford Instruments Channel 5 software. Misindexing (i.e. the wrong phase was allocated) and zero solutions (i.e. no phase identified) are concentrated at grain boundaries. Noise reduction and removal of zero solutions was performed following the procedure of Prior et al. (2002) and Bestmann & Prior (2003). Misindexing in both feldspars and micas was checked against EDS data and corrected during post-processing. Pole figures are upper hemisphere equal-area projections using one point per grain to avoid the over representation of large grains.

Three stitched EBSD/EDS maps were collected using the Zeiss EVO MA15 Scanning Electron Microscope (with NordleysNano high-sensitivity EBSD detector and Oxford Instruments Aztec Synergy EDS/EBSD) at Macquarie GeoAnalytical (Macquarie University, Sydney). An acceleration voltage of 20KeV, working distance of ~12mm and specimen tilt of 70° was used. Step sizes were 6-12um. Samples were prepared and post processed as above.

Whole Rock Geochemistry

Ten representative samples of rock components were separated from three samples of migmatite (LMC05, LMC06, LMC07) using a rock saw and grinding wheel. Weathered surfaces were removed and samples were washed thoroughly before being coarsely crushed (<1cm³) in a thick plastic sleeve using a rock hammer. Fragments were then reduced to a fine powder using a tungsten carbide barrel and ring TEMA mill. Care was taken to wash the mill components thoroughly between samples using ethanol and Milli-Q water to avoid contamination. Each powder was then separated into three to be prepared for the following analyses: (i) XRF major and trace element analysis, (ii) solution ICP-MS trace and rare earth element (REE) analysis, (iii) LA-ICP-MS trace and rare earth element analysis on fused glass discs.

X-ray Fluorescence (XRF)

Whole rock major and trace element data was collected on the PanAnalytical PW2400 WDXRF Spectrometer at the Mark Wainwright Analytical Centre, University of New South Wales, Australia. For major element analysis, 1g of sample powder was mixed with 10g of lithium borate flux then heated to 1050°C for 15 minutes in a Pt/Au crucible. The molten mixture was then poured into a 40mm Pt/Au casting dish, which cooled forming a glass disc. For trace element analysis, 10g of sample powder was mixed with 1g of ceridust (wax) binder. This mixture was then pressed into a pellet to be analysed. Loss on ignition (LOI) was determined by heating the samples to 1050°C for 1 hour.

Solution Inductively Coupled Plasma – Mass Spectrometry (ICP-MS)

Solution ICP-MS analysis of rare earth and trace elements was completed at Macquarie GeoAnalytical, Macquarie University, Sydney. 0.1g of each sample powder was measured into clean Teflon beakers before being digested using the following method: (i) Concentrated HF and HNO₃ were added, then heated on a hot plate at 150°C for 24 hours before being left to dry. (ii) This step was repeated for concentrated HF and HNO₃, then for the following acid combinations:

(iii) HF + HClO₄, (iv) 6N HCL. Samples appeared to have small amounts of carbon and hard to digest, refractory phases. The following steps were used to digest them: (v) To digest carbon, the sample was digested in a 6.5:2.5:1 mixture of HClO₄ (60%), HNO₃ (65%) and H₂O, and 10mL HF (40%) at 150°C for 72 hours, then dried. (vi) To digest refractory phases such as spinel and rutile, the sample was digested in 2mL HF with 0.3mL HCl and 0.3mL HClO₄ at 150°C for 24 hours, then dried. (vii) Finally, 6N HNO₃ was added and heated at 150°C for 24 hours, but not allowed to fully dry. Each sample was then diluted to 1:1000 in 2% HNO₃ + 0.25% HF. 0.5mL of each sample dilution was spiked with 0.02mL of a 6Li, As, Rh, In, Tm and Bi solution. The spiked samples were run on an Agilent 7500cs quadrupole ICP-MS. The calibration standard was BCR-2. 1:1000 and 1:5000 spiked dilutions of standards BCR-2, BHVO-2, BIR-1 along with blanks of HNO₃ and the spike were run throughout analysis.

Laser Ablation - Inductively Coupled Plasma – Mass Spectrometry (LA-ICP-MS)

Trace and rare earth element data was also obtained through LA-ICP-MS analysis of fused glass discs, providing a complimentary set of data to the solution ICP-MS data in section 3.5.2. While the solution ICP-MS data is generally more precise, this method allows for a more accurate determination of elemental concentrations in phases that are not easily digestible (such as zircon). Fused glass discs were made by combining 0.5g sample powder and 1.5g lithium borate flux. This was heated in a titanium crucible at 1050°C for 22 minutes. A small amount of ammonium iodide was added at 20 minutes to reduce the viscosity. The resulting molten material was then poured onto a heated carbon die and quench pressed into a thin glass disc. Standard BHVO-2 was prepared in the same way to run with samples. Discs were then stacked and fastened with epoxy before being mounted in epoxy and cut in half to expose all disc centres for ablation. Samples were analysed by an Agilent 7700cx quadrupole ICP-MS attached to a Photon Machines Excite Excimer laser ablation system at Macquarie GeoAnalytical (Macquarie University, Sydney). Each run was conducted at 100% power using a spot size of 110µm. Helium gas was run through the system for one minute before each ablation to record the background. Two-minute raster ablation lines were run across each sample. Standard NIST610 (Norman, 1996) was used as the calibration standard and run systematically through the analysis along with standards BHVO-2, AGV1, BCR-2. CaO (from XRF analysis) was used as the internal standard to allow for quantification of elemental concentrations. Data was processed in the GLITTER™ software (Griffin et al., 2008).

3. Field relationships

Migmatite rocks surveyed on Lynoch Station are exposed in several 10-20m², topographically flat outcrops; six outcrops were studied in detail (Fig. 2A). The migmatite broadly classifies as metatexite based on inferred low degrees of partial melting of a metapsammitic protolith (Fig. 2B, C. Craven et al., 2013; Brown, 1973; Sawyer, 2008). The most prominent feature of all outcrops and hand samples studied is several generations of leucocratic veins and dykes that cut dark- and light-coloured bands in the host rock to form vein-structured metatexite (Fig. 2B, Fig. 3, Fig. 4, Fig. 5A).

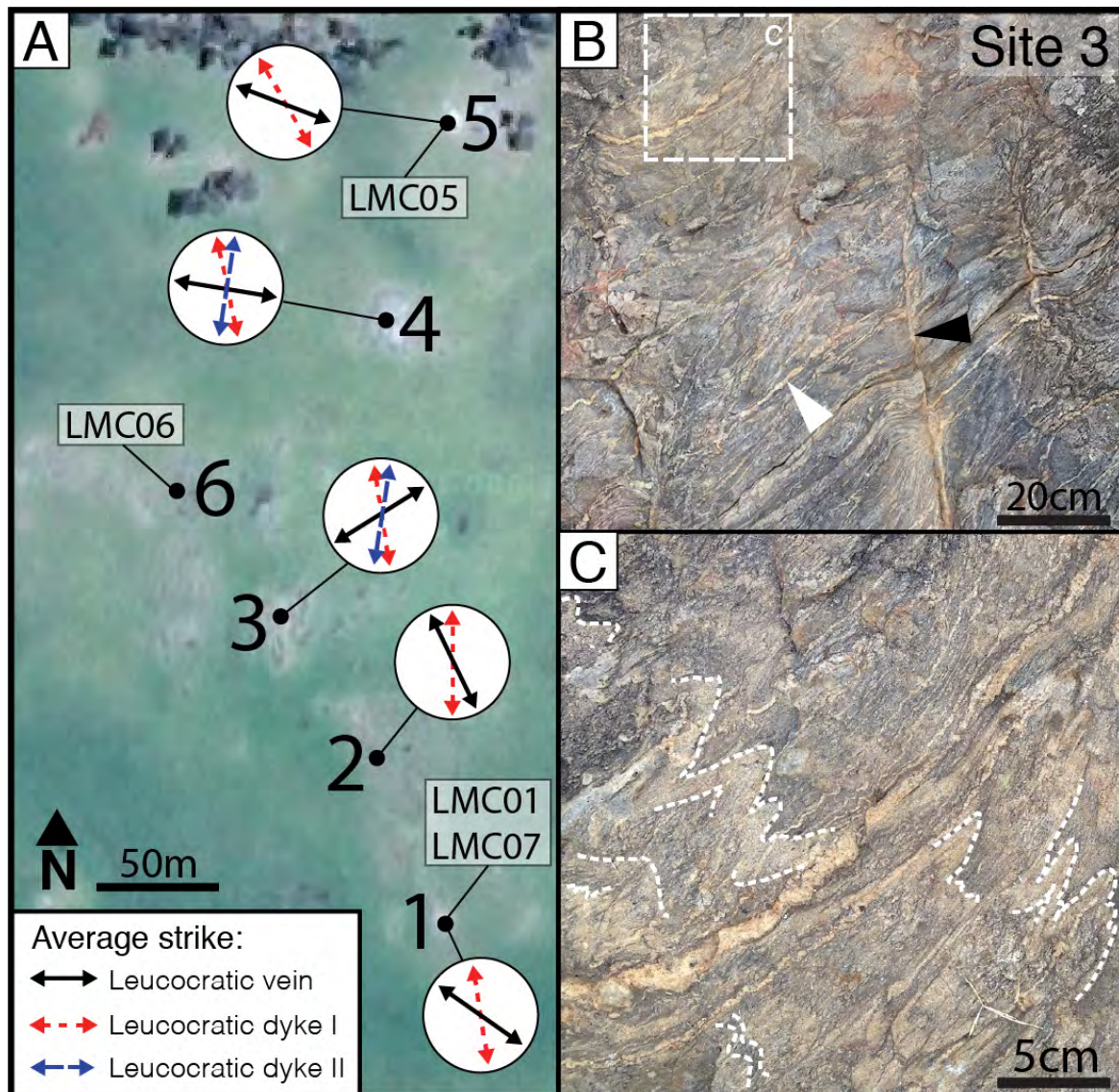


Fig.2. (A) Location of six migmatite sites (area corresponds to Fig. 1) surveyed in detail on Lynoch Station, showing average strike of leucocratic veins and two groups of leucocratic dykes. Where measured, veins and dykes are steep to sub-vertical. Samples used in this study are marked in white boxes. (B) Outcrop photograph from site 3 showing representative migmatite with leucocratic vein (white arrow) and leucocratic dyke I (black arrow). (C) Zoom of Fig. 1 (b) showing folded dark and light banding cut by leucocratic veins.

Table.1: Summary of leucocratic vein and dyke characteristics

Component	Strike	Spacing	Thickness	Length/Extent	Shape	Grain size	Composition
<i>Leucocratic vein</i>	commonly NNW	regular <0.03m	0.1-1cm	continuous	uniform thickness	fine <0.5cm	qz+plg+ksp
<i>Leucocratic dyke I</i>	NNW	irregular ~0.3m	0.1-3cm	10-50cm	lenticular	medium 0.5-2mm	ksp+qz+mu
<i>Leucocratic dyke II</i>	NNE	irregular <10m	10-100cm	continuous	undulating edges	coarse <5mm	mu+bt+qz+fsp

To aid interpretation and communication of results, the migmatite outcrops and samples are divided into five components: (i) light- and (ii) dark-coloured host, (iii) leucocratic veins and two types of leucocratic dyke (iv & v) distinguished by orientation, thickness and spacing (Table 1; Fig. 3). The terms vein and dyke in this study provide a distinction between the thinner pervasive leucocratic material and thicker, more variable, cross-cutting leucocratic material (see component map, Fig. 3), respectively. Leucocratic veins are generally thinner, finer grained, continuous across outcrop and composed of quartz and plagioclase. Leucocratic dykes are thicker, coarser grained, cut the pervasive leucocratic veins, discontinuous across outcrops and granitic in composition (K-feldspar–plagioclase–quartz ± mica; Table 1). Some thicker veins have a granitic composition like the leucocratic dykes. The term ‘leucocratic’ follows that of Sawyer (2008), describing a light crystallised portion of rock resulting from the injection of an anatectic melt into another rock within the zone of anatexis. This term is used here in favour of leucosome as the leucocratic portions do not meet the defined criteria for in-situ or in-source leucosomes, as discussed later. The term host is used in favour of mesosome, palaeosome or other nomenclature to represent the metasedimentary portion of the migmatite. These five components are described in detail below.

(i & ii) Light and dark host

The host component is fine grained, banded, grey-brown metapsammitic schist (Figs 1–5), comprising mainly quartz, K-feldspar, plagioclase and aligned biotite which defines the schistosity. The schist is heterogeneous in appearance, dominantly comprised of light-coloured grey-brown schist with subordinate mm- to cm-scale variably darker-coloured bands (Figs 2C, 3A,B, 4A,C, 5A,C, 6). The darker-coloured bands are commonly aligned sub-parallel to the leucocratic veins and dykes (Figs 4A,C, 6). However, the darker-coloured bands appear to cut some leucocratic components in places (Figs 5A,C, 6B). The boundaries of the darker-coloured bands also vary, being smooth and even (Fig. 5A), diffuse (Fig. 5B) or jagged (Fig. 5A,C), and tapering out into fine fingers (black arrow Fig. 5A). Leucocratic veins show mutually cross-cutting relationships with the

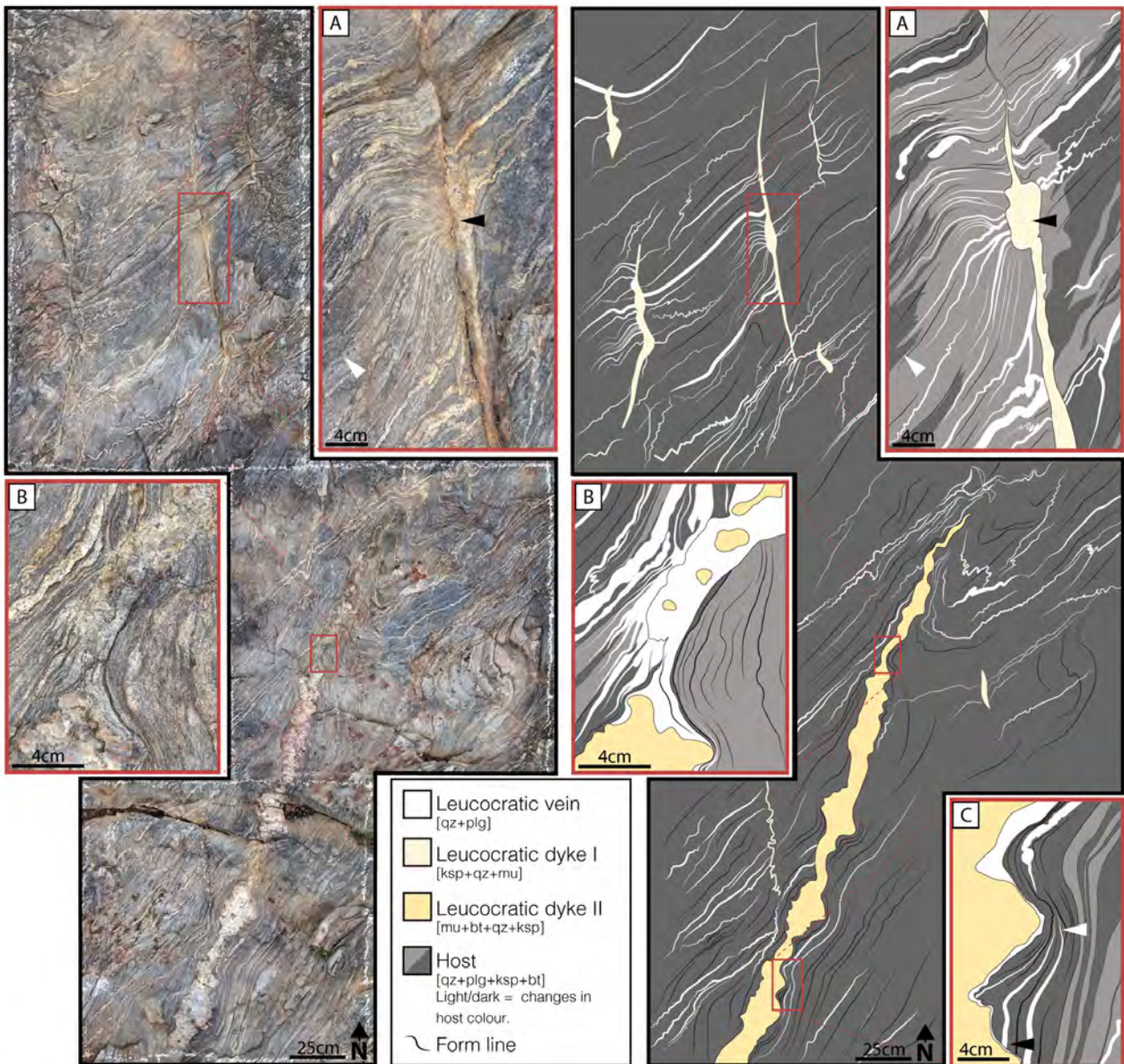


Fig.3: Outcrop photographs (left) and corresponding component maps (right) of site 3. (A) leucocratic veins (diagonal bottom-left to top-right) are cut by a NNW-striking leucocratic dyke I. The thicker part of the leucocratic dyke (black arrow) contains coarse (<2mm) K-feldspar (ksp) and quartz (qz). Dark and light banding in the host is sub-parallel to leucocratic veins (white arrow). Note the asymmetry in leucocratic vein density either side of the leucocratic dyke. (B) Leucocratic dyke II, striking NNE, contains coarse (<5mm) grains of K-feldspar (ksp) and quartz (qz). In a boudin-like structure, the dyke loses coherence and appears as a string of large grains surrounded by a finer, quartz and feldspar. (C) Leucocratic dyke II ‘pinches and swells’ with the leucocratic veins both conforming to (white arrow) and being cut by (black arrow) the undulating surface.

darker-coloured banding (Fig. 5C). Leucocratic veins that intersect the darker-coloured host bands fall into two groups: (i) some veins become indistinct or heavily ghosted in the dark band (Fig. 5C), while others (ii) do not change character across both the light- and dark-coloured bands. Light grey elongate K-feldspar porphyroblasts (<3mm long) define a pervasive foliation across the left half of sample LMC06, occurring in both light and dark host bands (the foliation is marked by light-grey

dashed lines on Fig. 5A). The orientation of this foliation is sub-perpendicular to the light/dark banding (left side of Fig. 5A), but may be locally transposed to be sub-parallel in other places (centre of Fig. 5A).

Leucocratic veins and dykes

Leucocratic veins and dykes are abundant in the studied metatexite migmatite, making up an average of 12.5% of the total outcrop (Fig. 3). Due to the topographic flatness of the outcrops, only the strike of these components could be measured reliably (Fig. 2A). Where measured, veins and dykes are steep to sub-vertical. The individual characteristics and relationships of the leucocratic components are summarised in Table 1 and detailed below.

(iii) Leucocratic veins

Thin (0.1-0.5cm) leucocratic veins are pervasively spaced (<3cm) across all outcrops (Figs. 2–6). The leucocratic veins are coarser in grain size compared to the host components and are dominantly composed of quartz and plagioclase. The leucocratic veins vary from gently/openly folded, with a wavelength of ~60cm (e.g. site 1; Fig. 4A) to wiggly/ptygmatic (e.g. site 4. Fig. 4C), to straight (e.g. site 5; Fig. 4D). Most veins are well defined with an even width, while others are a ‘string’ of grains connected by a fine seam of quartz (Fig. 6A). These grains are generally elongate and aligned axial planar to folds of the ‘string’. Rarely fine (mm- to sub-mm-scale) domains of mafic selvage line the boundaries of some leucocratic veins and dykes (arrows in Fig. 6B). These occur on one or both sides of the vein or dyke and are dominantly composed of biotite. Slightly thicker (~1cm) leucocratic veins, that contain K-feldspar in addition to quartz and plagioclase, are observed parallel to the dominant plagioclase-quartz veins.

(iv) Leucocratic dyke I (NNW trending)

Thin (0.1-3cm) leucocratic dykes cut the leucocratic veins, locally disturbing the orientation of leucocratic veins in complex patterns (Fig. 3A, Fig. 4B–D). These dykes display variable thickness along strike, have tapered ends (Fig. 3), are 10-50cm long and irregularly spaced at ~30cm intervals. At outcrop-scale, these dykes have a dominant NNW-strike (Fig. 3). However, in hand sample, multiple directions are observed (Fig. 5B). The complex disturbance to the orientation of leucocratic veins across an outcrop is more pronounced close to leucocratic dykes and decreases away from them until deviations are indiscernible from the average strike of the veins throughout the outcrop (Fig. 3). At some points along a leucocratic dyke, the leucocratic veins either side of it

may converge to form a ‘pucker’-like structure (Kreigsman, 2001; Kisters et al., 2009; Figs 3A, 4C,D). An asymmetry is apparent in places involving more leucocratic veins on one side of a leucocratic dyke compared to the other (Fig. 3A). Leucocratic dykes are coarser in grain size when compared to leucocratic veins and are composed of K-feldspar+quartz+plagioclase+muscovite. The widest part of these dykes (e.g. black arrow in Fig. 3) is normally dictated by a few large <1.5mm K-feldspar, quartz & muscovite grains, whereas the tapered ends are composed of finer sub-mm quartz and feldspar.

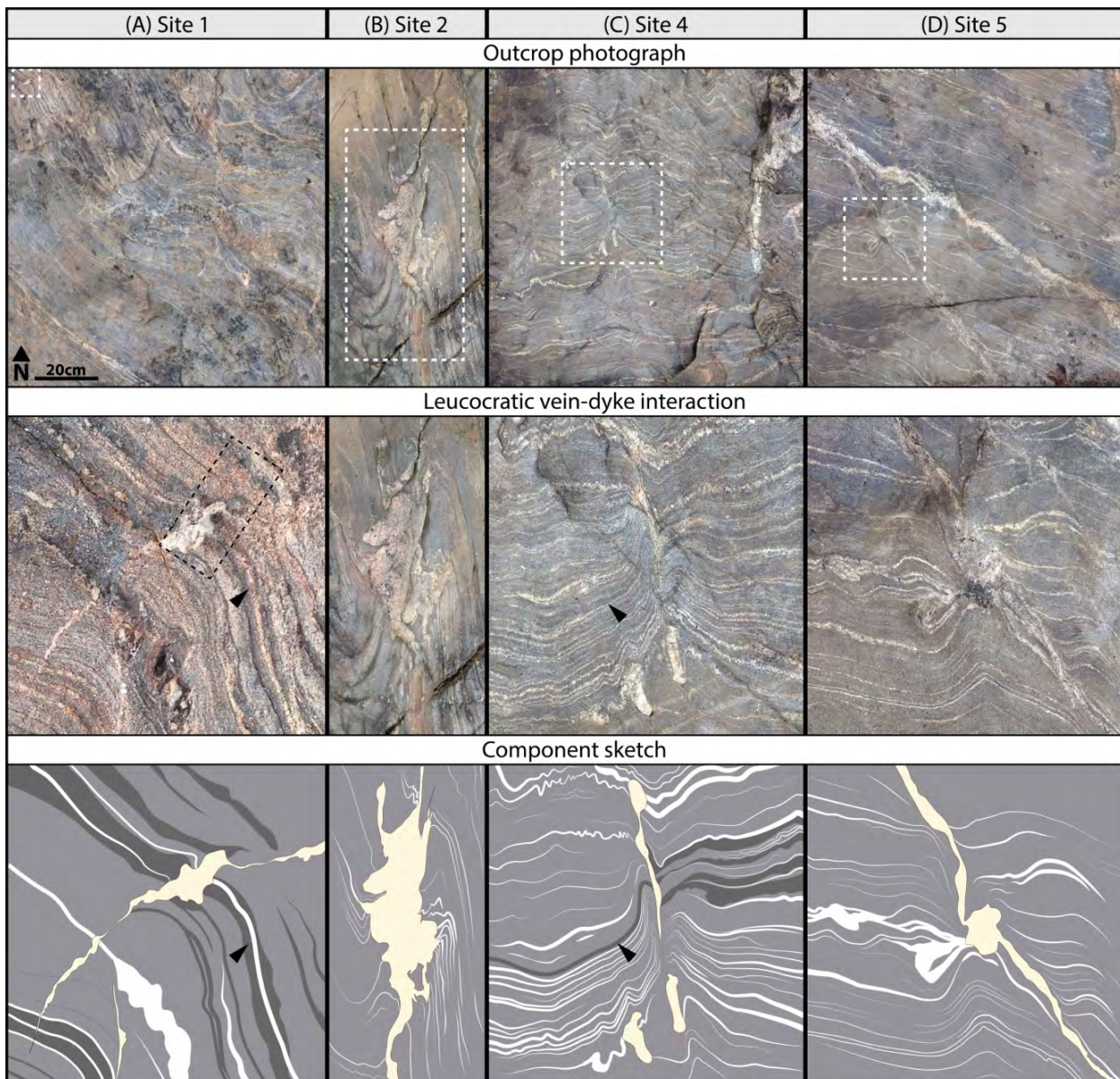


Fig.4: Top row shows metre-scale outcrop photos for sites 1, 2, 4 & 5, that give context to the detailed photos (middle row) and component sketches (bottom row). Note, proximal to the leucocratic dykes, the complex localised deviation in the orientation of leucocratic veins (A–D) and dark bands in the host (black arrows; A,C). Note: thin section LMC01C-A is taken in-situ from site 1 (black dashed rectangle). Component colours are the same as Fig.3.

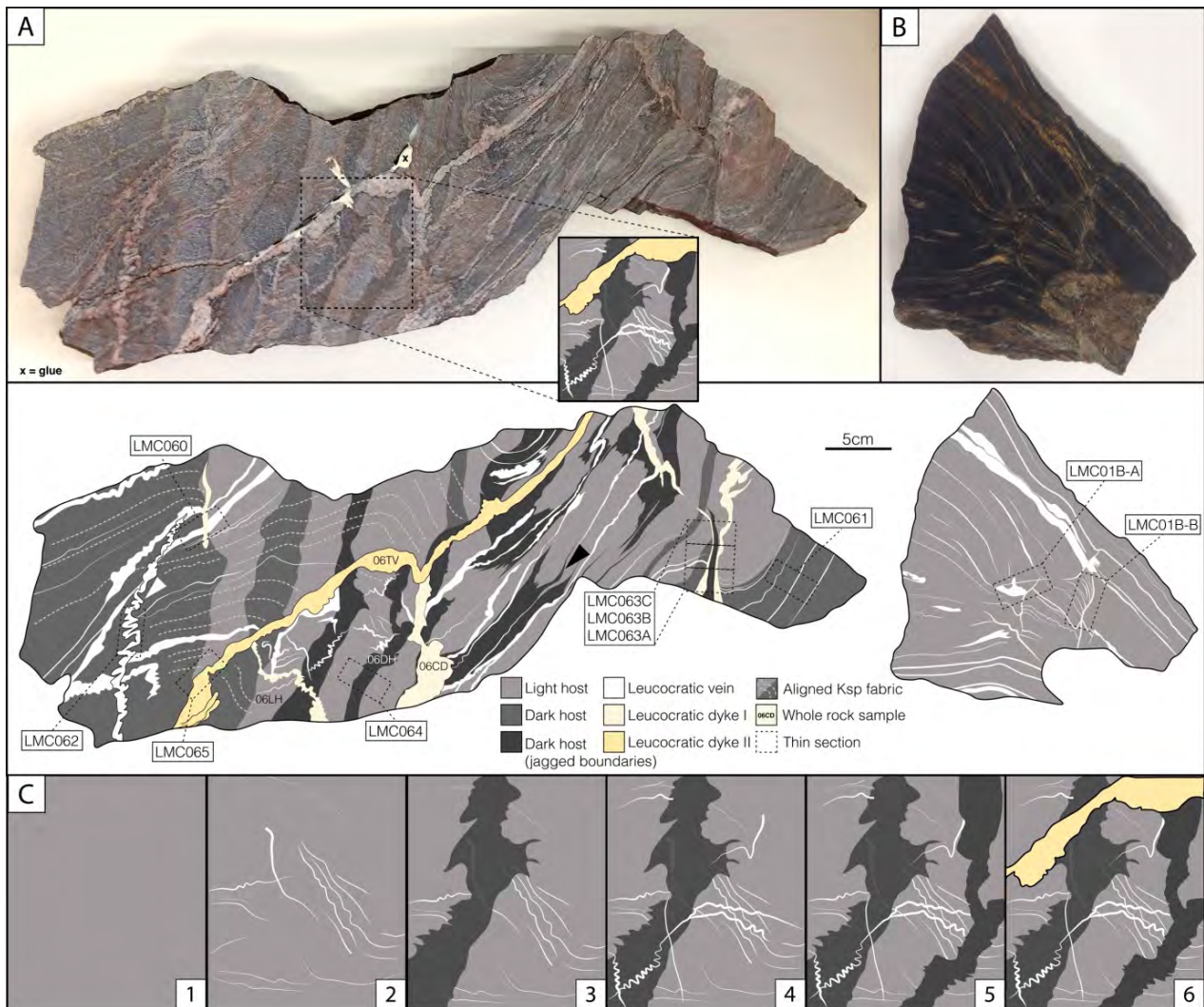


Fig.5. Photograph and corresponding component sketch of two unoriented hand samples; sample shown in (A) LMC06 (location in Fig. 2) was collected by Kim Jessop (current PhD student at Macquarie University). This sample was cut in half with one side used to cut eight thin sections (black dashed rectangles) and to separate components for whole rock analysis (four components labelled 06LH, 06DH, 06TV, and 06CD). (B) Complex array of multiple leucocratic dykes in hand sample. Rock was cut in half using an oil saw (so colour appears very dark). Two thin sections were cut (black dashed rectangles). (C) Interpreted sequence of mutually cross-cutting relationships between veins, dykes and dark-coloured bands in the host. Light-coloured host (stage 1) is cut by leucocratic veins (stage 2), in turn cut by dark-coloured band (stage 3), more leucocratic veins, some ptygmatic (stage 4), a darker-coloured band (stage 5) and a leucocratic dyke (stage 6).

(v) Leucocratic dyke II (NNE trending)

Thicker (0.1-1m) leucocratic dykes trend NNE, at approximately 60° to the first set of leucocratic dykes, and are observed throughout the field area (Fig. 2, Fig. 3). These are coarser grained compared to all other migmatite components and are mainly composed of K-feldspar, plagioclase, quartz, muscovite and biotite. The dykes are generally consistent in width but some taper out over several metres. The edges may undulate on a cm scale (Fig. 3C), the shape dictated by coarse

>5mm grains or aggregates. These dykes may be oriented sub-parallel to leucocratic veins, which conform in places to the dykes undulating edges (Fig. 3B, 3C). An intersection between the two groups of leucocratic dykes was rarely observed at the outcrop-scale. However, the hand sample LMC06 contains an intersection of two dykes (Fig. 5A), but the leucocratic components are complex and the assignment of the outcrop-scale component definitions are tentative in Figure 5A. In sample LMC06, a thick (<2cm-wide) K-feldspar-rich dyke (bottom left to top right, Fig. 5A) has a mm-scale biotite selvage that cuts light/dark host banding and earlier veins and dykes. The generally straight orientation of this thick vein contains an isolated fold (centre Fig. 5A), where a more diffuse, sub-perpendicular wiggly vein intersects it. The result is an apparent ‘pull’ in the direction of the intersecting vein, creating a localised fold. The orientation of the pervasive light grey mineral fabric also deviates in this area towards the wiggly vein. Samples of leucocratic dyke II were not able to be collected in the field due to the very flat outcrops.

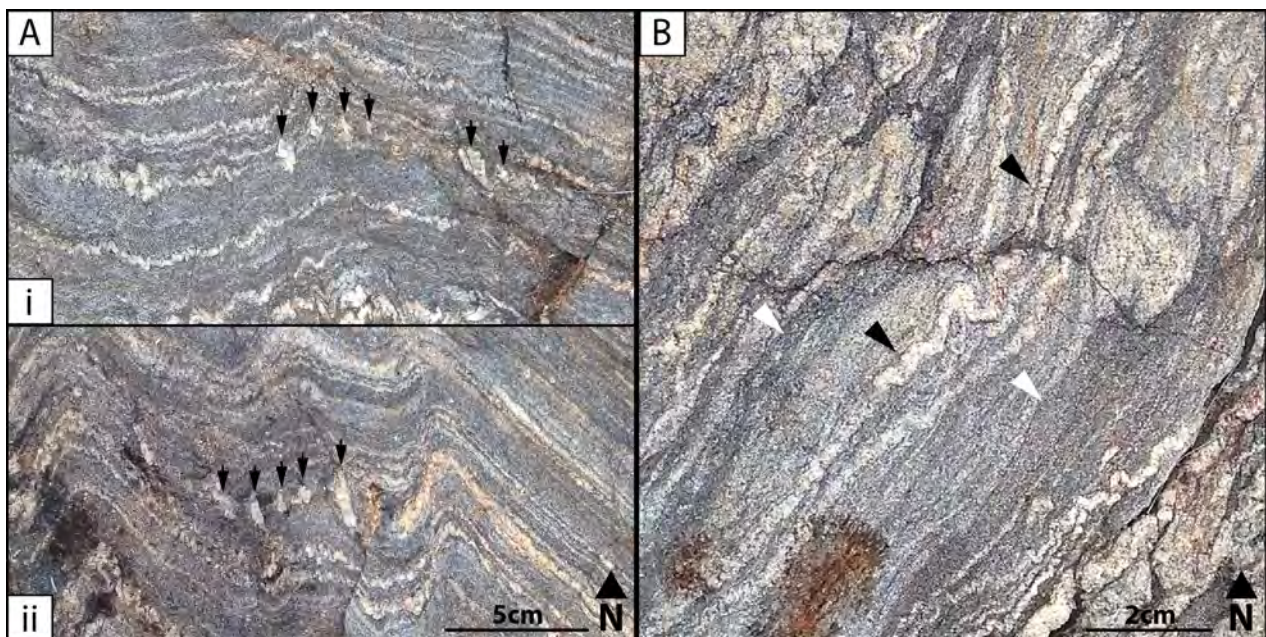


Fig.6: Field photographs of numerous dark- and light-coloured bands in host rock component. (A) Site 4: Coarse elongate grains (black arrows) within leucocratic veins are aligned at a high angle to the vein trend and are axial planar to the open folds. (B) Site 3: Rare mm- to sub-mm-scale biotite-rich selvage (black arrows) lining both sides of a complexly folded leucocratic vein. Also note the irregular dark-coloured bands (white arrows) cutting through the host component and possibly across some leucocratic veins (upper right).

(vi) Other rare types of vein and dyke

Ptygmatic veins are observed rarely in both outcrop and hand sample (left, Fig. 5A). They are commonly 2mm wide and generally have the same overall strike as adjacent less-folded veins. They are composed of feldspar and quartz and have biotite selvages on both sides.

Patches or dykes of pegmatitic material (Fig. 4D) commonly occur oriented at a low angle to the leucocratic veins and are observed mainly at sites 4 and 5. At site 1, a coarse grained, garnet-bearing pegmatitic dyke is sub-parallel to the leucocratic veins. This dyke is 10cm wide with undulating edges and contains up to ~10 vol.% pale pink garnet. Garnet is only observed as rare single grains elsewhere in the field area (generally in the host near a leucocratic vein or dyke).

(vii) Cross-cutting relationships

Based on field relationships general cross-cutting relationships can be observed (e.g. Fig. 5C), allowing a general geological history to be reconstructed. (i) The light host component is interpreted to represent a protolith of psammitic composition (Fig. 5C-1). (ii) Intrusion of small irregular veins (Fig. 5C-2). (iii) Dark host band with irregular boundaries cuts earlier veins, 'ghosting' the portions that it cuts through (Fig. 5C-3). (iv) More veins intrude, cutting the dark host band and earlier veins. Some of these veins vary between straight and ptygmatic along strike which could indicate that they have (a) been deformed by a regional compressive stress parallel to the ptygmatic portion length after emplacement (secondary folding, post-intrusion; Godfrey, 1954) or, (b) intruded with a higher injection pressure, causing a more competent vein to 'buckle' in a less competent host (syn-intrusion deformation; Wilson, 1952. Fig. 5C-4). (v) Another dark host band with irregular boundaries cuts the earlier features sub-parallel to the first dark host band (Fig. 5C-5). (vi) A leucocratic dyke cuts through all features, forming a biotite rich selvage at its boundaries (Fig. 5C-6).

4. Petrographic and microstructural analysis

Petrographic and microstructural analysis of 17 polished thin sections was completed using optical microscopy and back-scatter electron imaging. To communicate results and allow a correlation between the outcrop scale and the microscale, each thin section will be subdivided into four components of the migmatite: (i) light- and (ii) dark-coloured host, (iii) leucocratic vein, and (iv) leucocratic dyke I (no samples were obtained for leucocratic dyke II). Most thin sections include a

cm-scale leucocratic vein and/or dyke within variable host rock. Other sections were cut to characterise single migmatite components, such as those analysed for XRF whole rock analysis.

Fig. 7 summarises the grain size, mode and mineral assemblage of representative samples of migmatite components, illustrating the variation within and between different components.

(i) Light host

The fine grained (0.01-0.8mm) metapsammitic light-coloured host migmatite component is composed of varying modes of quartz, plagioclase, biotite, K-feldspar with minor muscovite and apatite (Fig. 7, Fig. 8). Quartz and plagioclase are the dominant phases, accounting for 70-80 vol.%.

Grain size	Modal distribution	Mineral	Mode
Light host	05H 0.03-0.5 mm	Quartz	27.0
		Plagioclase	42.5
		K-feldspar	10.5
		Biotite	19.5
		Muscovite	0
		Apatite	0.25
	06LH 0.05-0.3 mm	Quartz	40.0
		Plagioclase	30.0
		K-feldspar	14.0
07H 0.02-0.8 mm	Biotite	12.0	
	Muscovite	4.0	
	Apatite	0.3	
	Quartz	37.5	
	Plagioclase	43.5	
	K-feldspar	3.0	
Dark host	06DH 0.1-1.2 mm	Biotite	15.5
		Muscovite	0
		Apatite	0.2
		Quartz	4.0
		Plagioclase	41.5
Thick leuc. vein	06TV 0.2-1.8 mm	K-feldspar	13.0
		Biotite	25.5
		Muscovite	15.0
		Apatite	1
		Quartz	53.0
	07TV 0.01-1.8 mm	Plagioclase	34.0
		K-feldspar	11.0
Leucocratic dyke	05CD 0.3-2.5 mm	Biotite	2.0
		Muscovite	0
		Apatite	0.1
		Quartz	76.5
		Plagioclase	21.0
	06CD 0.2-2.4 mm	K-feldspar	1.7
		Biotite	0.7
Leucocratic dyke	05CD 0.3-2.5 mm	Muscovite	0
		Apatite	0.1
		Quartz	28.0
		Plagioclase	13.5
		K-feldspar	54.5
		Biotite	3.5
	06CD 0.2-2.4 mm	Muscovite	0
Apatite		0.2	

Fig. 7: Summary of grainsize, mode and mineral assemblage for representative samples of migmatite components: (i) light- and (ii) dark-coloured host, (iii) leucocratic veins, and (iv & v) leucocratic dykes. Mineral modes were acquired using ImageJ. Numbers are an average of several areas sampled for each component across all available thin sections. Host components do not include vein or dyke material.

Quartz is generally anhedral with a slightly larger average grain size compared to adjacent plagioclase. Anhedral plagioclase grains often form interconnected networks around quartz (Fig. 8A). Biotite occurs throughout the host (12-20 vol.%) and is aligned to define a schistosity that is sub-parallel to leucocratic veins. Higher concentrations of biotite occur as selvages directly adjacent and parallel to leucocratic veins and dykes (Fig. 8B) or as irregular dark bands (called dark-coloured host and described next). Biotite grains become darker, coarser and less well-aligned closer to leucocratic dykes (~10mm either side; Fig. 8C). The proportion of K-feldspar varies more than any other mineral in the host. Some areas contain <1 vol.% small (<0.2mm) interstitial K-feldspar (Fig. 8D) while others have ~14 vol.% medium grains with irregular boundaries. Some mm-scale almost monomineralic bands of anhedral K-feldspar (>80 vol.%) occur sub-parallel to leucocratic veins (Fig. 8D). Rare microcline twinning is observed. Muscovite is absent in much of the host, but is locally rich adjacent to some veins and dykes. When present, it occurs as thin elongate grains that make up <5 vol.% of the host. Very fine anhedral to almost round apatite grains (<0.05mm) are common. The concentration and grain size varies with a noted increase in size and abundance close to some leucocratic dykes, thick veins and ptygmatic veins (Fig. 8E). These apatite grains occur as inclusions in coarse biotite (black arrows Fig. 8E) and as individual grains in the matrix (white arrows Fig. 8E). Less than 3mm-wide pseudomorphed relict grains occur in some samples and contain a mix of predominantly K-feldspar with muscovite, quartz and biotite (e.g. LMC06 – Fig. 8F). These are present in both the light and dark host. In the light host, the relict grains have significantly less K-feldspar when compared to those in the dark host. Elongate biotite and muscovite anastomose around the relict grains, creating a pattern resembling an S-C' fabric within the dark host (Fig. 8F).

(ii) Dark host

The dark-coloured host migmatite component occurs in irregular bands (~1-4cm wide) that are composed almost entirely of plagioclase (40-60 vol.%) and biotite (25-50 vol.%) with aligned muscovite (~12 vol.%) and varying proportions of K-feldspar (0-14 vol.% - Fig. 7, Fig. 9). The boundaries of these bands are irregular to jagged, with small fingers jutting out sharply into the light-coloured host (Fig. 9A). Rare mm-scale aggregates of coarse grained plagioclase + muscovite + biotite occur in some dark-coloured bands (black arrow - Fig. 9B) and these may be along strike of leucocratic veins and connected by a thin 'ghosted' quartz + plagioclase vein (red dashed lines – Fig. 9C). The ghosted portion of vein has a considerably higher abundance of plagioclase, biotite and muscovite, and lower abundance of quartz relative to the vein in the adjacent light-coloured

host. Quartz grains within the dark-coloured host are commonly much smaller (<0.1mm) and less abundant (<4 vol.%) compared to those in the adjacent veins and light-coloured host (Fig. 7, Fig. 9D). Some samples (e.g. thin section LMC063B) lack K-feldspar, being composed entirely of plagioclase (60 vol.%), biotite (30 vol.%) and muscovite (10 vol.%), while other samples of dark-coloured host (e.g. thin section LMC064) contained abundant (~14 vol.%) anhedral (black arrow – Fig. 9E) and interstitial (white arrow - Fig. 9E) K-feldspar.

Table 2: Comparison of leucocratic vein and dyke characteristics for the samples analysed. Note 1: thicker and coarser grained examples were observed in the field. Note 2: no samples of Leucocratic dyke II were collected.

Type		Thickness (mm)	Grain size (mm)	Mineral mode (%)						
				qz	plg	ksp	bt	mu	ap	
<i>Leucocratic Vein</i>	a	Qz-rich	<1.0	0.01-0.8	>75	<25	-	1	-	-
	b	qz+plg	<1.0	0.05-0.4	58	41	-	1	-	<1
	c	qz+plg+ksp	<2.5	0.05-1.2	55	20	22	3	-	-
<i>Leucocratic Dyke I</i>	a	ksp-rich	<5.0	0.5-2.5	30	14	50	3	2	1
	b	qz-rich	<2.0	<1.0	>80	6	5	2	5	2

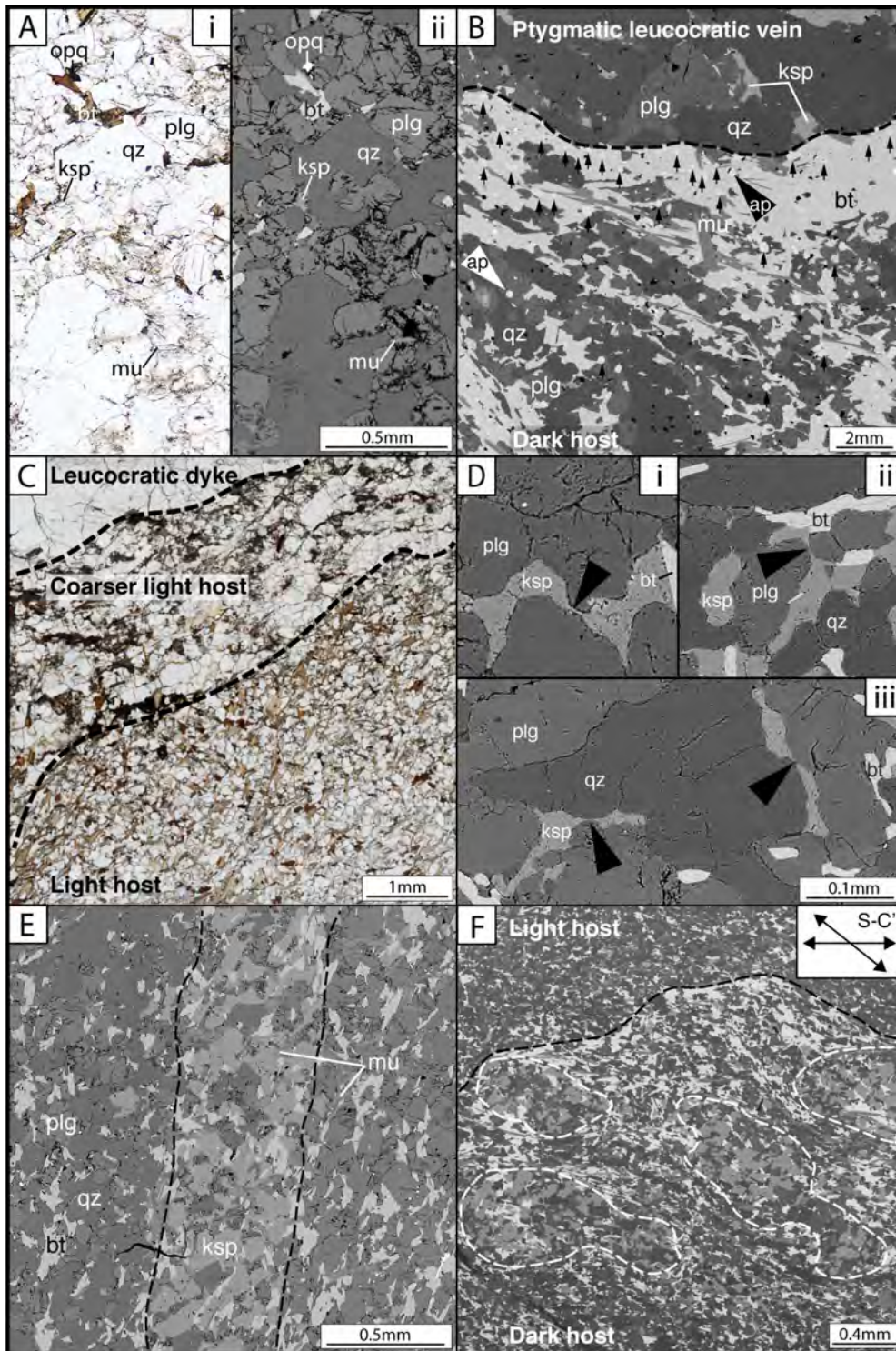


Fig. 8: (A) Plane polarised light (PPL) photomicrograph and backscatter electron (BSE) image of plagioclase and quartz within light host component (sample LMC01C-A). Note how plagioclase forms a connected network around the quartz grains. (B) BSE image of increased grain size and mode of biotite and apatite proximal to a ptygmatic leucocratic vein (sample LMC062). (C) PPL photomicrograph of increased grainsize in host where proximal to a leucocratic dyke I (sample LMC01B-B). (D) BSE images of K-feldspar with interstitial texture and as films between grain boundaries of plagioclase and/or quartz (sample LMC064). (E) BSE image of an anhedra K-feldspar-rich band through host (sample LMC01C-A). (F) BSE image highlighting the S-C'-like fabric formed by anastomosing biotite and muscovite around relict grains containing K-feldspar+muscovite+quartz+biotite. The black dashed line indicates a contact between light- and dark-coloured host bands (sample LMC065).

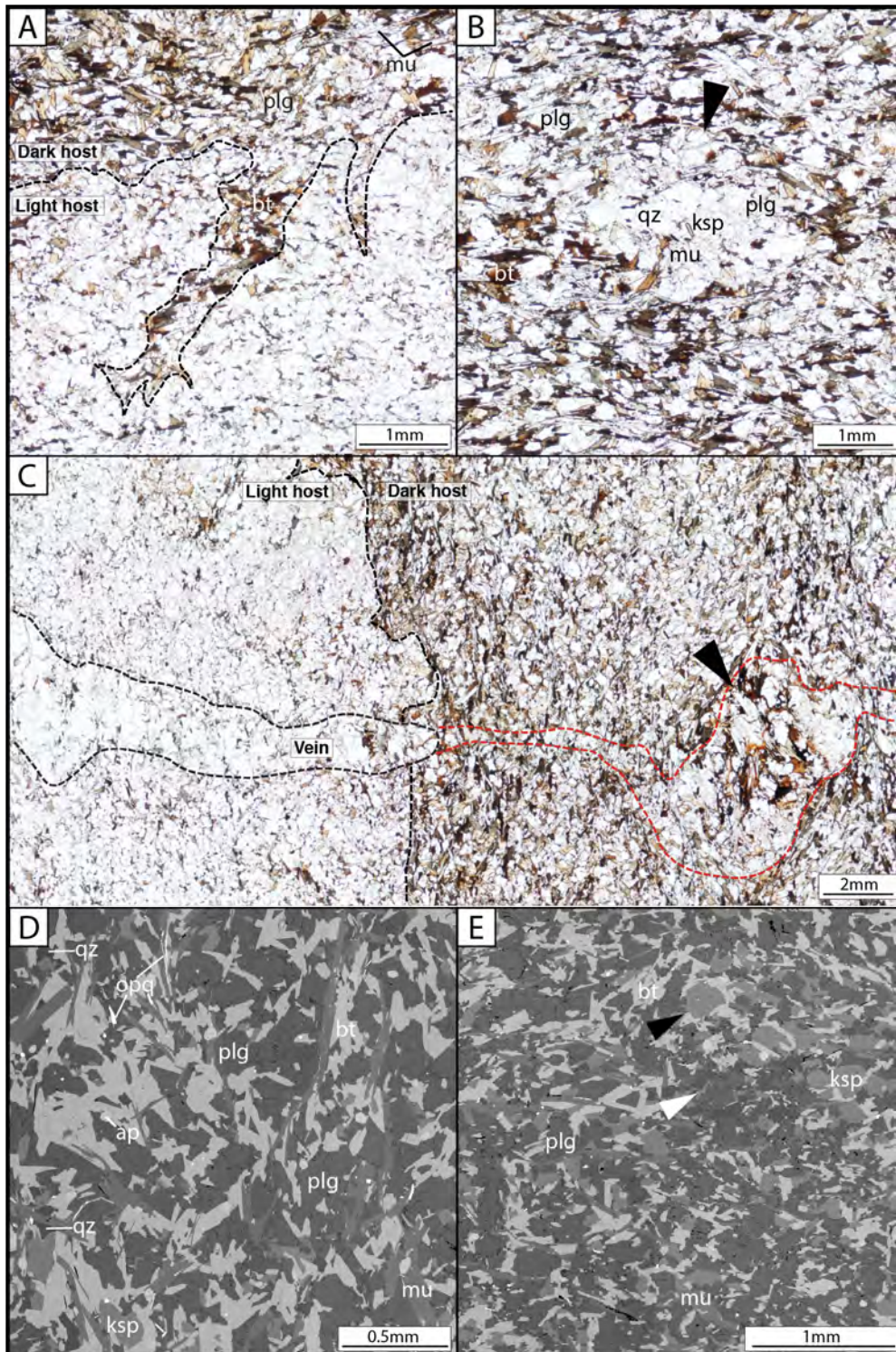


Fig. 9: PPL photomicrographs of (A) jagged dark-coloured host boundary protruding into light-coloured host (sample LMC064). Note: dark-coloured host is rich in biotite and muscovite. (B) Coarse grained felsic mineral aggregate within the dark host (sample LMC064). (C) Leucocratic vein cut by a dark host band (sample LMC064). A coarse-grained aggregate of plagioclase+muscovite+biotite+quartz (black arrow) is along strike of the vein, possibly a modified relict of the vein where it was enriched in mica during formation of the dark-coloured host. A trail of slightly larger quartz grains can be traced between the vein and aggregate (red dashed lines). (D) Very small (<0.1mm) quartz grains in a very low (<4 vol.%) abundance. (E) K-feldspar bearing dark host. K-feldspar occurs as larger anhedral grains (black arrow) and smaller interstitial grains (white arrow).

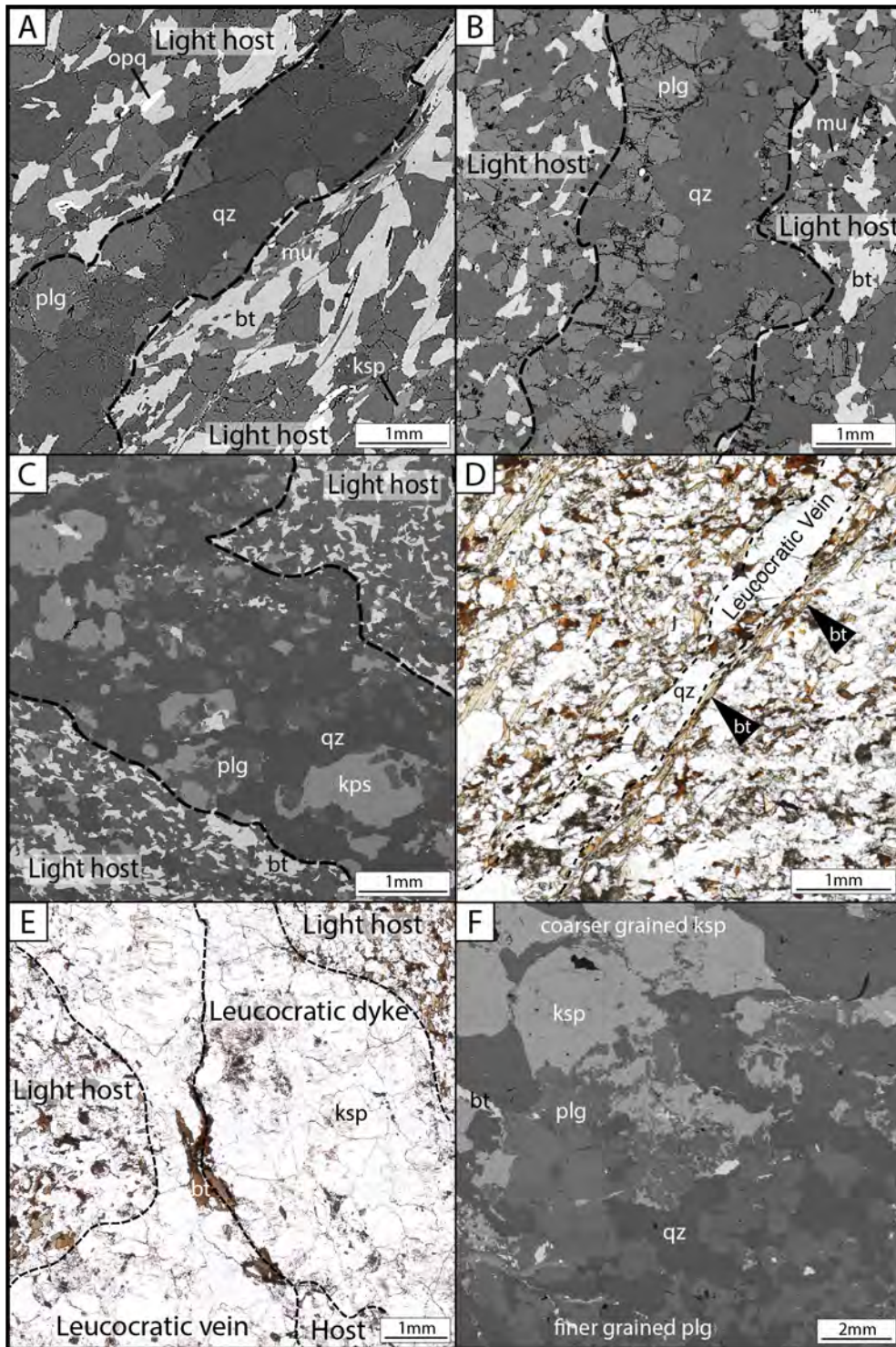


Fig. 10: BSE images showing that leucocratic veins range from being rich in (A) quartz (sample LMC01B-B) to (B) quartz+plagioclase (sample LMC01C-A) to (C) quartz+plagioclase+K-feldspar (sample LMC05C-A). Note asymmetric distribution of minerals: (B) quartz on one side and plagioclase on the other; and (C) coarse K-feldspar grains are located dominantly on one side. (D) PPL photomicrograph showing quartz-rich vein with biotite-rich selvage on one side (black arrows; sample LMC01B-B). (E) PPL photomicrograph showing large biotite grain at the contact between K-feldspar bearing leucocratic vein with diffuse boundaries and leucocratic dyke I (sample LMC05C-A). (F) BSE image showing fine-grained plagioclase has pseudomorphed coarse grains of K-feldspar at the contact between a quartz+plagioclase vein composition along strike from a quartz+plagioclase+K-feldspar vein composition (sample LMC065).

(iii) Leucocratic vein

The leucocratic vein components of the migmatite include three distinct compositional types (Table. 2): (a) quartz-rich leucocratic veins (Fig. 10A), (b) quartz+plagioclase leucocratic veins (Fig. 10B) and (c) quartz+plagioclase+K-feldspar leucocratic veins (Fig. 10C). Quartz-rich leucocratic veins have a blocky texture, with slightly elongate grains aligned parallel to the fracture surface.

Plagioclase appears as a few isolated grains lining the edges of a nearly continuous quartz seam (Fig. 10A). Quartz+plagioclase and quartz+plagioclase+K-feldspar leucocratic veins show a blocky growth pattern, commonly with a different composition either side of the median line (Fig. 10B, Fig. 10C). Leucocratic veins may be bordered on one or both sides by mm to sub-mm scale, biotite-rich selvages (Fig. 10D). Large biotite grains are observed where leucocratic veins are cut by leucocratic dykes (Fig. 10E). Some leucocratic veins change composition along strike (e.g. quartz+plagioclase+K-feldspar to quartz+plagioclase). This change is associated with the pseudomorphous replacement of coarse K-feldspar grains by finer plagioclase grains (Fig. 10F).

(iv) Leucocratic dyke I

Leucocratic dyke components of the migmatite show two compositional types (summarised in Table. 2):

(a) Coarse K-feldspar-rich leucocratic dykes

Coarse grained (<2.5mm) K-feldspar (50 vol. %), quartz (30 vol. %) and plagioclase (14 vol. %) leucocratic dyke I compositions are the most common type of dyke (Table. 2). These large grains are irregularly shaped with embayed, high energy boundaries (Fig. 11A, Fig. 11B). Quartz aggregates in the dyke have sutured boundaries and mottled extinction, indicating some minor recrystallisation overprints a dominantly igneous character (Fig. 11C). The largest plagioclase grains occur as highly fragmented, rounded aggregates, with trails of finer plagioclase cutting across the large K-feldspar grains (e.g. thick leucocratic veins Fig. 10F). The large K-feldspar and quartz grains contain sparse finer-grained inclusions of anhedral to almost round plagioclase and quartz spread evenly throughout. Inclusions of biotite are found within K-feldspar proximal to the dyke-host boundary (Fig. 11A). In smaller dykes (<3mm wide), large single grains of K-feldspar or quartz may span the entire width of the dyke (Fig. 11E). Median lines are observed rarely, often with strings of fine interstitial quartz with low dihedral angles (black arrows Fig. 11D). While the distribution of minerals is commonly even throughout a dyke, in some areas the coarse-grained dyke mineral assemblage mirrors the dominant mineral in the adjacent finer grained host (Fig. 11E).

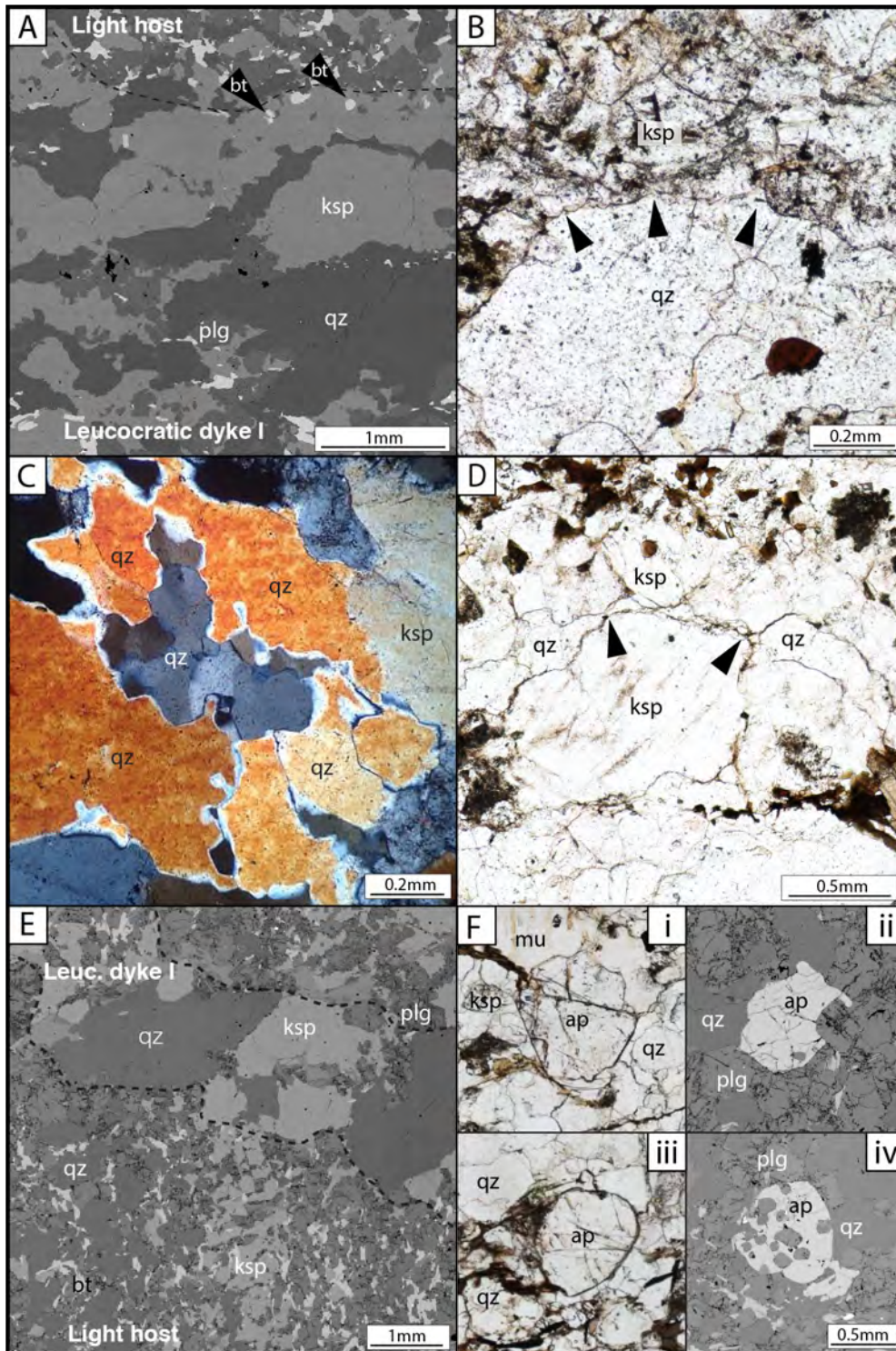


Fig.11: (A) BSE image of representative K-feldspar-rich leucocratic dyke I composition and texture (sample LMC05C-A). Note biotite inclusions within the large K-feldspar grains next to host. (B) PPL photomicrograph of K-feldspar embayments or bulges into large quartz (sample LMC01C-A). (C) Crossed polarised light (XPL) photomicrograph of quartz with sutured boundaries and mottled extinction (sample LMC01C-A). Slide is thicker than 30 microns so quartz appears orange. (D) PPL photomicrograph of a grain boundary film or seam of quartz showing low dihedral angles along the median line of K-feldspar-rich dyke (sample LMC05C-A). (E) BSE image of leucocratic dyke I and light host showing the growth of K-feldspar and quartz in dyke mimicking the dominance of these phases in the host (F) PPL photomicrographs and BSE images of different apatite grains occurring in leucocratic dyke I (samples LMC01C-A [i&iii] & LMC01B-B [ii&iv]).

For example, K-feldspar is more common in a dyke where there is abundant K-feldspar in the host rock (e.g. Fig 11E). Approximately 1mm wide apatite grains (some poikilitic) are spaced evenly (~15mm) along some samples of dyke (Fig. 11Fii & iv).

(b) Medium-fine quartz-rich leucocratic dykes:

A finer grained, quartz-rich composition is observed in shorter, thinner leucocratic dykes (e.g. sample LMC01B-B, Fig. 5). These are generally composed of up to 80 vol.% medium grained (<1mm) quartz. Interspersed throughout the dyke are large <4mm muscovite (5 vol.%) and biotite grains (2 vol.%).

(v) Other rare types of veins and dykes

(b) Ptygmatic vein:

The ptygmatic vein examined in sample LMC062 has almost identical mineral and mode distribution as the leucocratic dyke I (K-feldspar-rich) as well as the textures and relationships between minerals. These include the serrated contacts between large quartz and K-feldspar grains. It is surrounded by a biotite-muscovite-apatite-rich selvage which can be seen in hand sample to be up to 4mm wide on both sides of the vein. Poikiloblastic biotite directly adjacent the vein is extremely coarse (<5mm), fining in grain size moving away from the vein. This biotite contains abundant inclusions of <1mm rounded ~0.1mm apatite grains (Fig. 8B). These apatite grains up to 0.3mm are also found throughout this selvage.

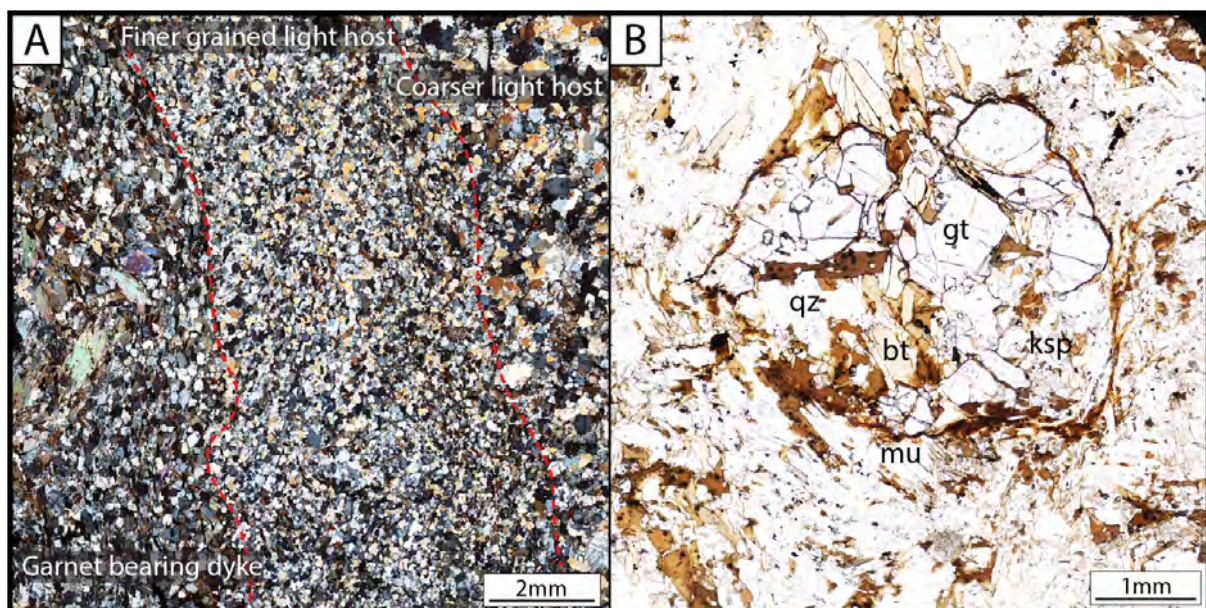


Fig. 12: (A) Cross-polarised light (XPL) photomicrograph of finer grained host band directly adjacent and parallel to garnet bearing dyke (sample LMC01-gt). (B) Plain polarised light (PPL) photomicrograph of a partially replace garnet grain by biotite, quartz, K-feldspar and muscovite (sample LMC01-gt).

(c) Garnet bearing vein

Located at site 1, this ~10cm wide garnet bearing dyke is composed of muscovite (30 vol.%), biotite (30 vol.%), quartz (15 vol.%), feldspar (15 vol.%) and garnet (10 vol.%). The dyke has a ~1-2mm zone of finer grains at its edge (Fig. 12A). Muscovite is poikilitic with corroded grain boundaries. Garnet grains are large (<8mm), fragmented and are commonly partially replaced by other minerals such as biotite (Fig. 12B). Biotite is weakly aligned sub-parallel to the dyke fracture surface, anastomosing around the large garnet grains (Fig. 12B).

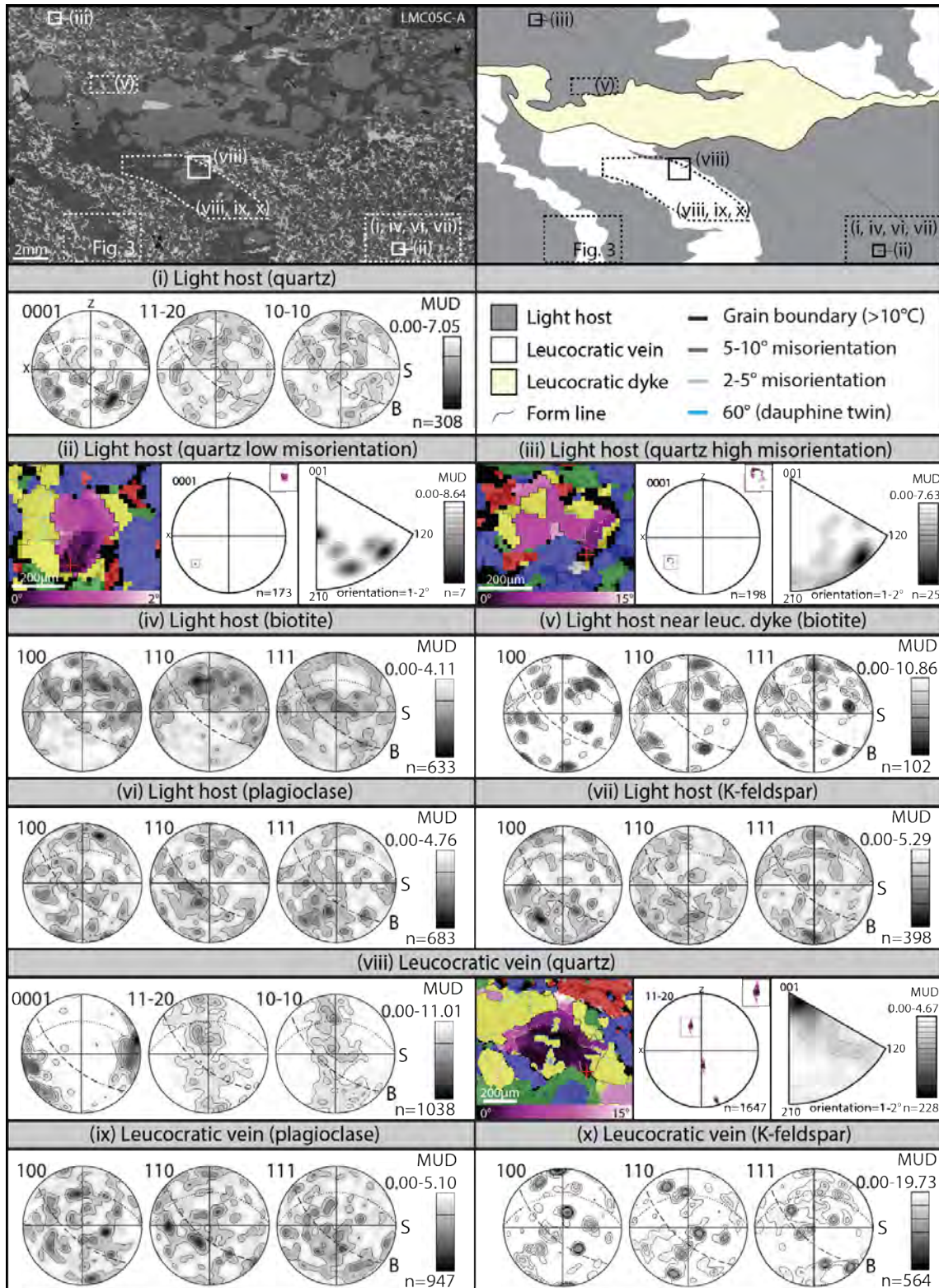
5. Quantitative Orientation Analysis using Electron Backscatter Diffraction (EBSD)

EBSD microstructural analysis was undertaken to further characterise the light/dark host, vein and dyke components, focussing on crystallographic preferred orientation (CPO), the relationship of crystal orientations relative to each other and internal lattice distortion of grains. 24 EBSD maps were taken across six representative thin sections (LMC01C-A, 01B-B, 05B-A, 05C-A, 064, 065). Overall, quartz and biotite show marked trends in both CPO and internal misorientation within and between components. Plagioclase and K-feldspar have scattered CPOs and low internal misorientation in most samples.

Due to the nature of these structures (coarse grains in small scale features), a limited number of grains are present for analysis in some cases. Pole figures were constructed using one point per grain except where showing internal grain misorientation scatter.

Light host

Light host quartz is randomly oriented in most samples (e.g. sample LMC01C-A, 05B-A, 05C-A, Fig. 13i). An exception to this is strongly aligned light host quartz within thin section LMC064, where [0001] is 45° to X-axis (dark host – light host boundary plane) (Fig. 14i). The internal orientation spread of individual randomly oriented quartz grains within the light host is generally less than 2.5° (Fig. 13ii). Rare quartz grains have an anomalously high internal misorientation with a systematic dispersion along a small circle (<15°, Fig. 13iii). Finding a correlation between these rare grains and their location is uncertain, with a seemingly random distribution throughout the light host. The average quartz misorientation in the aligned light host is ~5° but grains with an internal misorientation <12° are observed (sample LMC064, Fig. 14i). Compared to leucocratic veins and dykes, the light host generally has a higher frequency of Dauphine twins and less low angle boundaries (LAB). Biotite within the light host has a strongly aligned CPO, with the basal plane



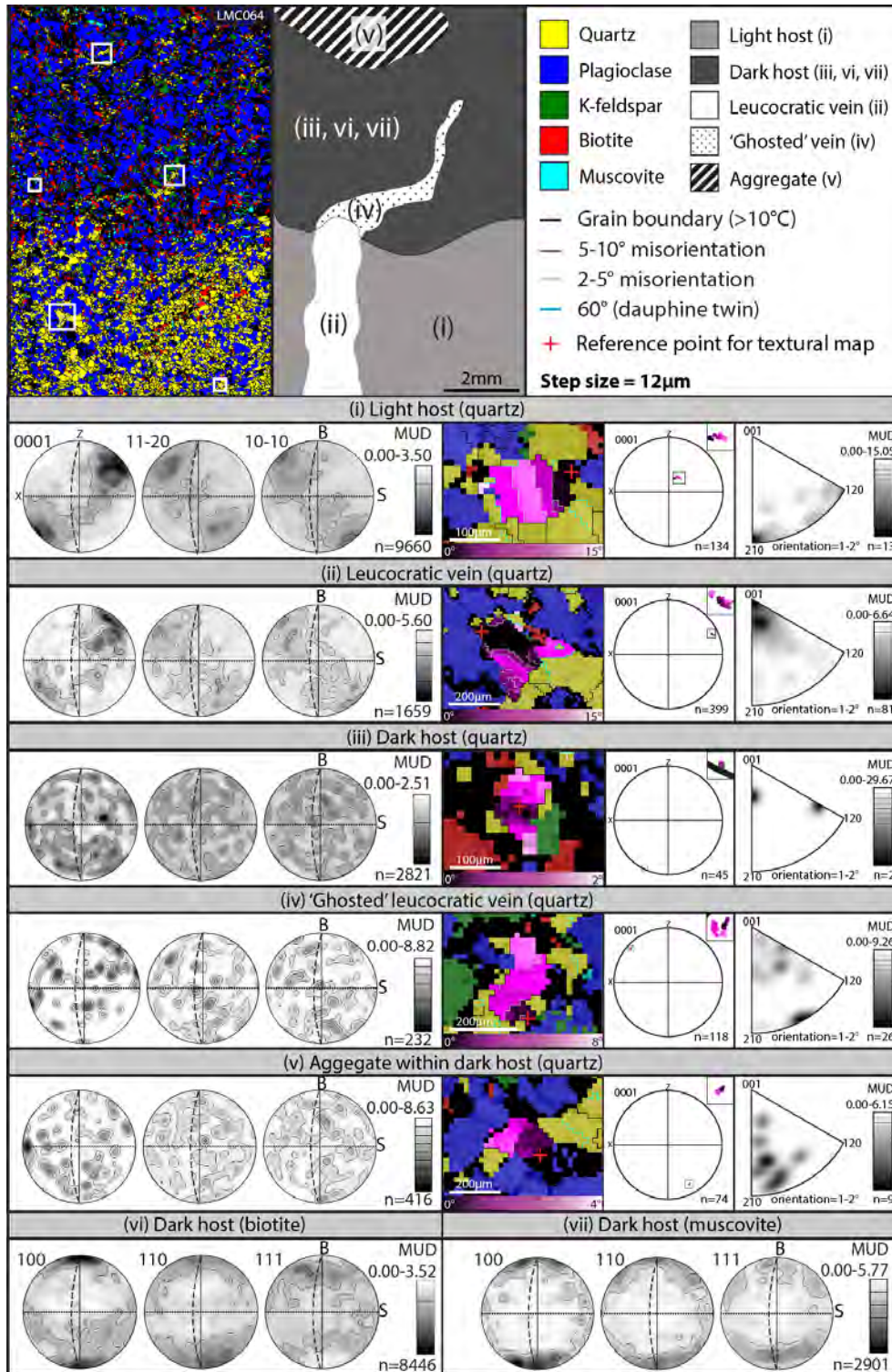


Fig. 14: EBSD phase map and component map of light host, dark host, leucocratic vein and ghosted leucocratic vein. Pole figures are sampled for the entire area show for each component in the phase map. Pole figure contour lines = 1 MUD. Next to pole figures are EBSD texture maps of single quartz grains within that component (white boxes in phase map show where grains are), pole figure showing internal misorientation spread and inverse pole figure showing the misorientation in crystal frame for orientations between $1-2^\circ$. (i) Quartz grain within the light host, (ii) quartz grain within the dark host, (iii) quartz grain within a leucocratic vein, (iv) quartz grain within 'ghosted' portion of a leucocratic vein. In pole figure: Dotted line = dark host foliation plane (marked with S = foliation). Line with long dashes = trace of vein/host boundary (marked with B = boundary).

defining the host foliation and lying sub-parallel to the leucocratic dyke (Fig. 13iv). This alignment becomes slightly more scattered proximal to leucocratic dykes (Fig. 13v). Plagioclase and K-feldspar have a random CPO throughout the light host (Fig. 13vi, 13vii) and individual grains have a low internal misorientation ($<2^\circ$).

Dark host

Quartz grains are smaller ($<0.01\text{mm}$) and randomly oriented within the dark host (Fig. 14iii) compared to the adjacent light host. Internal misorientation of quartz grains within the dark host is very low ($<1.5^\circ$, Fig. 14iii). Quartz grains within the large aggregates of plagioclase+biotite+quartz+muscovite in the dark host show a very weak CPO with [0001] aligning parallel to dark host foliation (marked 'S' on pole figure Fig. 14v). Biotite and muscovite within the dark host are strongly aligned, with their basal planes defining foliation 'S' (Fig. 14vi & 14vii). Plagioclase and K-feldspar are randomly oriented and show low internal misorientation ($<2^\circ$) within the dark host. Feldspars and micas within the aggregates have similar properties to elsewhere in the dark host (i.e. random CPO, low internal misorientation for feldspars, aligned CPO for mica).

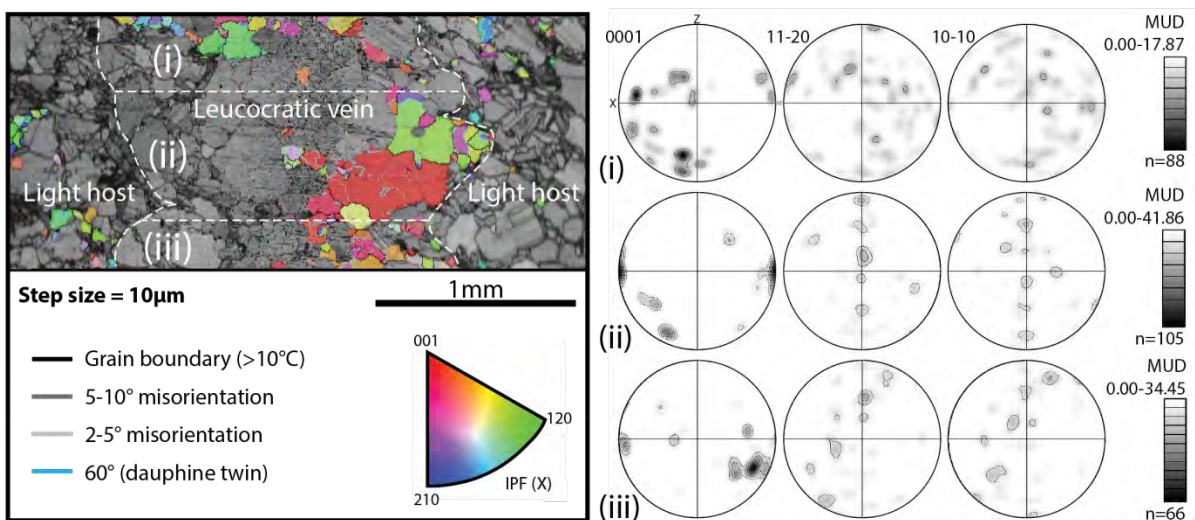


Fig. 15: EBSD band contrast map overlain with quartz orientation (Inverse Pole Figure X colouring). Quartz CPO analysis at hinge of folded leucocratic vein near leucocratic dyke I. Grain boundaries are marked. Pole figures i-iii correlate to the zones i-iii indicated by white dashed lines. Location of area marked in Fig. 13.

Leucocratic vein

Leucocratic vein quartz is strongly aligned with [0001] aligning sub-parallel to the light host foliation plane 'S' (Fig. 13viii, Fig. 14ii). A very minor rotation in quartz orientation is observed at fold hinges (Fig. 15). The orientation spread of individual quartz grains within veins varies greatly

(2-24°) though most grains have a ~5° spread (Fig. 14ii). The largest orientation spreads are observed within the largest quartz grains (Fig. 13viii). Leucocratic veins within the light host that intersect the dark host bands have an aligned quartz CPO ([0001] mimicking alignment of the adjacent host) and high internal misorientation (10-15°, Fig. 14ii). The ghosted portion along strike of this vein within the dark host has a random quartz CPO and low internal misorientation (<2°, Fig. 14iv). Plagioclase and K-feldspar grains within leucocratic veins are randomly oriented (Fig. 13ix, 13x). Plagioclase grains generally have an orientation spread <1.5°, while K-feldspar has an orientation spread of <2°.

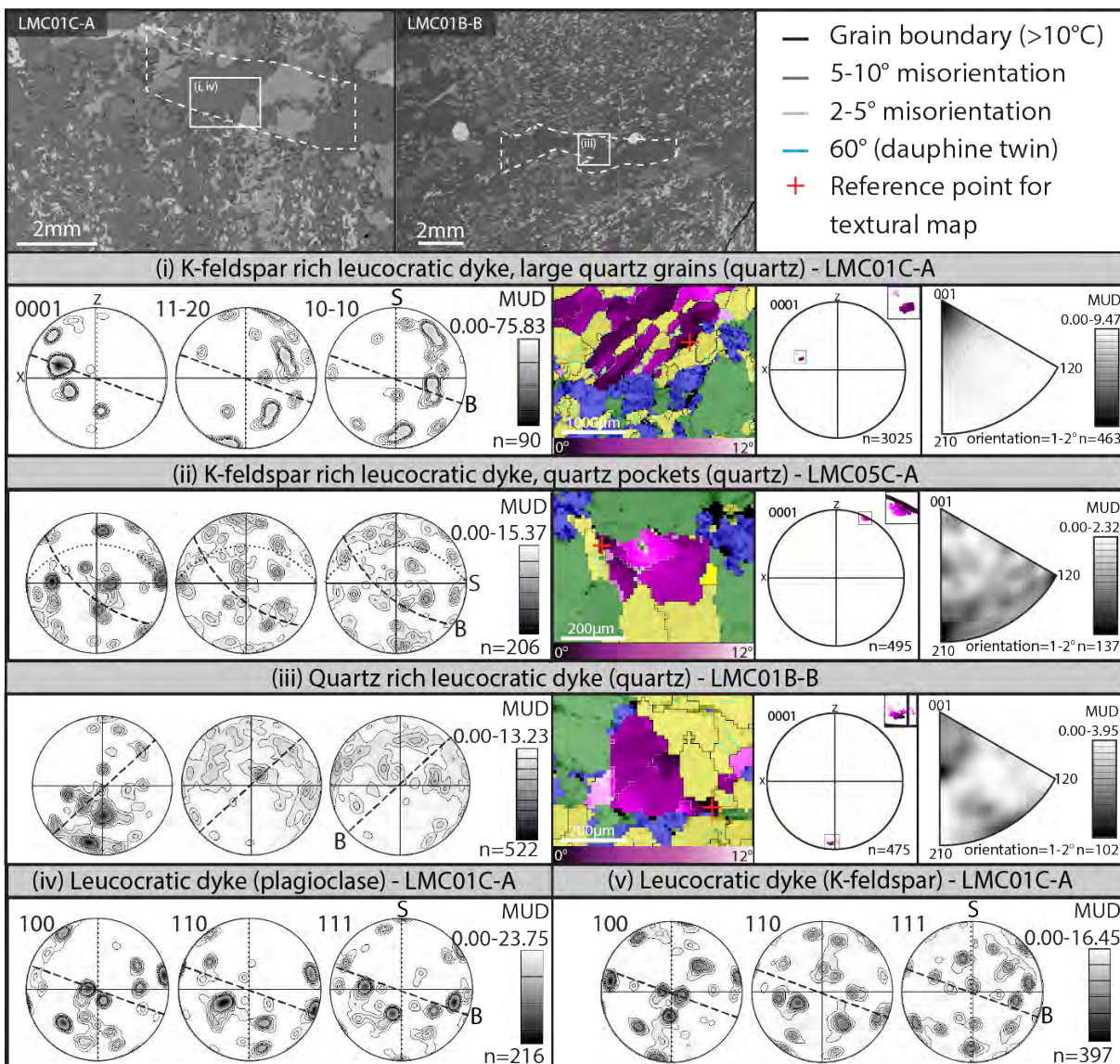


Fig. 16: (A) BSE image of sample LMC01C-A. Dashed area indicates where pole figure (i & iv) were sampled from. ii, iii & v were sampled from LMC05C-A (marked in Fig. 13). In pole figure: Dotted line = dark host foliation plane (marked with S = foliation). Line with long dashes = trace of vein/host boundary (marked with B = boundary).

Leucocratic dyke

Finding trends in leucocratic dykes between different samples is made difficult by the fact that (a) dyke composition and appearance is variable, (b) quartz distribution is highly irregular within dykes and (c) grains are quite large relative to the dykes sampled. In the K-feldspar rich dykes (the most common dyke composition), the largest grains (<4mm) are often oriented with [0001] perpendicular to the host foliation and parallel to the dyke strike direction (Fig. 16i). Sub-mm scale quartz pockets surrounded by coarse K-feldspar grains within these dykes have a random CPO (Fig. 16ii) and individual quartz grains have a high (<12°) internal misorientation (Fig. 16ii). Quartz [0001] within the quartz rich leucocratic dyke I (composition b) is generally aligned 45° to the leucocratic vein foliation plane and sub-perpendicular to the leucocratic dyke fracture surface (Fig. 16iii). Plagioclase and K-feldspar grains within the dykes have a random CPO and low internal misorientation (<2°, Fig. 16iv, 16v).

6. Whole rock geochemistry

Whole rock geochemical analysis was undertaken on ten sub-samples of migmatite components from three representative samples (five light host, one dark host, two leucocratic dykes, two thick leucocratic veins – summarised in Table 3). The major and trace element contents of the four components analysed in this study are compared to a compilation of existing data including (1) low-grade metasedimentary rocks from the Wongwibinda Metamorphic Complex, and two local granitoid plutons of the Hillgrove Plutonic Suite: (2) Abroi Granodiorite and (3) Wongwibinda 2-mica granite (Farrell, 1992; Henson, 2000; Kim Jessop, personal communication, 2017; Appendix 1). The average value for the metasedimentary rocks is plotted with 1 standard deviation.

Table 3: Whole rock major and trace element concentrations for separated rock components. Major element oxides are presented as oxide wt.%. Trace elements are presented as ppm. The analysis method used to obtain each element is shown. L.O.I. = Loss on ignition.

	<i>Light host</i>				<i>Dark host</i>	<i>Leucocratic dyke</i>		<i>Thick leucocratic vein</i>		Method	
	05H1	05H2	06LH	07H1	07H2	06DH	05CD	06CD	06TV		07TV
SiO₂	65.9	67.4	73.1	68.6	69.1	55.1	82.7	75.8	78.4	83.2	XRF
TiO₂	0.6	0.6	0.5	0.6	0.6	1.1	0.1	0.3	0.1	0.1	XRF
Al₂O₃	15.4	15.1	12.0	14.7	14.2	20.0	9.3	12.1	12.1	9.1	XRF
Fe₂O₃	4.7	4.4	3.4	4.3	4.0	7.6	0.5	2.1	0.7	0.4	XRF
Mn₃O₄	0.1	0.1	0.1	0.1	0.1	0.1	0.0	0.0	0.0	0.0	XRF
MgO	1.5	1.5	1.1	1.3	1.2	2.5	0.2	0.6	0.2	0.1	XRF
CaO	2.1	2.2	1.4	2.2	2.6	2.4	1.9	1.6	2.0	1.6	XRF
Na₂O	4.1	4.2	3.3	4.1	4.4	4.8	3.6	3.8	4.7	3.5	XRF
K₂O	4.0	3.5	2.9	3.2	1.7	4.8	0.3	2.4	0.9	0.3	XRF
P₂O₅	0.1	0.1	0.1	0.1	0.2	0.3	0.0	0.2	0.2	0.1	XRF
L.O.I.	0.9	0.6	1.1	0.7	0.7	1.2	0.2	0.6	0.6	0.4	XRF
Total	99.5	99.7	98.9	100.1	98.7	100.1	98.9	99.5	99.9	98.9	
Li	30.1	26.4	22.3	25.4	23.9	44.3	4.0	13.4	5.5	2.8	Solution
Be	3.0	2.7	2.1	2.1	2.7	1.9	3.2	1.6	1.7	1.6	Solution
Sc	14.1	12.5	9.7	12.1	12.2	20.5	2.4	6.6	2.8	1.9	Solution
V	68.0	65.7	43.8	66.0	59.6	137.1	8.9	26.5	10.9	3.1	Solution
Cr	24.6	23.1	22.8	22.2	20.8	61.1	5.0	13.1	16.9	3.3	Solution
Co	78.7	73.3	88.3	84.3	84.4	39.9	157.4	117.5	150.0	158.6	Solution
Ni	11.3	10.3	12.2	9.6	10.2	24.5	4.2	10.0	8.0	4.4	Solution
Cu	9.4	11.3	16.2	8.7	7.8	16.7	17.3	17.9	27.5	18.0	LA-ICP-MS
Zn	87.3	78.8	62.8	72.8	69.2	124.6	12.1	36.9	13.5	11.4	Solution
Ga	18.6	17.6	13.1	16.6	16.4	25.3	9.9	11.7	10.6	8.0	Solution
Rb	167.7	152.0	94.9	125.4	93.6	140.6	16.5	59.0	19.8	10.1	Solution
Sr	274.1	271.3	166.1	249.1	227.2	226.0	184.4	190.7	206.2	155.0	Solution
Y	22.7	21.4	26.1	22.7	24.8	63.9	9.7	23.9	25.5	11.2	LA-ICP-MS
Zr	248.5	237.1	286.5	259.0	246.2	333.0	22.2	116.0	115.6	114.9	LA-ICP-MS
Nb	11.7	9.0	7.7	9.3	9.5	18.2	1.5	4.2	1.0	0.8	Solution
Mo	0.3	0.5	0.3	0.4	0.5	0.4	0.2	0.3	0.4	0.3	Solution
Cd	0.1	0.1	0.0	0.1	0.1	0.1	0.1	0.0	0.1	0.0	Solution
Ag	0.4	0.2	0.3	0.1	0.2	0.2	<0.192	0.2	0.6	3.4	LA-ICP-MS
Sn	13.3	10.5	16.2	11.4	10.0	16.4	61.8	19.7	89.3	19.2	LA-ICP-MS
Cs	11.4	9.4	6.6	3.9	3.6	14.5	1.2	3.7	1.3	0.5	Solution
Ba	586.6	549.0	647.9	769.7	256.1	721.1	35.9	556.1	147.6	100.3	Solution
La	54.2	42.6	27.3	28.2	29.2	51.2	14.3	17.2	15.7	12.1	Solution
Ce	69.8	71.4	57.0	60.5	59.6	114.4	19.6	36.5	32.9	23.3	Solution
Pr	12.0	9.3	6.9	6.9	7.1	14.4	2.8	4.5	4.0	2.7	Solution
Nd	45.1	34.6	25.7	25.0	25.8	57.7	10.2	17.0	15.5	9.8	Solution
Sm	8.6	6.8	5.3	5.1	5.3	12.3	2.1	3.9	3.8	2.1	Solution
Eu	1.7	1.5	1.4	1.4	1.3	2.0	0.7	1.3	1.2	0.8	Solution
Gd	7.7	6.3	4.8	4.6	4.9	10.9	2.1	3.8	4.0	2.2	Solution
Tb	1.1	0.9	0.7	0.7	0.8	1.6	0.3	0.6	0.7	0.4	Solution
Dy	5.5	4.7	4.0	4.0	4.5	8.4	1.8	3.5	4.1	2.2	Solution
Ho	1.0	0.9	0.8	0.9	0.9	1.6	0.3	0.7	0.8	0.5	Solution
Er	2.6	2.3	2.3	2.4	2.7	4.3	0.9	2.2	2.4	1.4	Solution
Tm	0.3	0.3	0.4	0.4	0.4	1.0	0.1	0.4	0.5	0.4	Solution
Yb	1.9	1.7	2.1	2.2	2.4	3.7	0.7	2.2	2.1	1.2	Solution
Lu	0.3	0.3	0.3	0.3	0.4	0.5	0.1	0.3	0.3	0.2	Solution
Hf	6.4	6.2	7.7	6.8	6.5	9.0	0.5	3.3	2.4	4.3	LA-ICP-MS
Ta	1.1	0.9	0.8	0.9	1.0	1.5	0.5	0.6	0.4	0.5	Solution
Au	36.9	12.2	35.2	25.9	20.8	33.8	27.0	25.6	53.7	29.4	LA-ICP-MS
Pb	13.4	11.4	17.0	14.6	10.6	19.6	9.0	17.5	14.8	16.0	LA-ICP-MS
Th	15.1	14.6	13.0	13.0	13.7	25.2	2.7	7.8	6.2	5.1	Solution
U	1.9	1.7	2.6	1.3	1.4	4.7	0.5	1.4	1.5	1.1	LA-ICP-MS

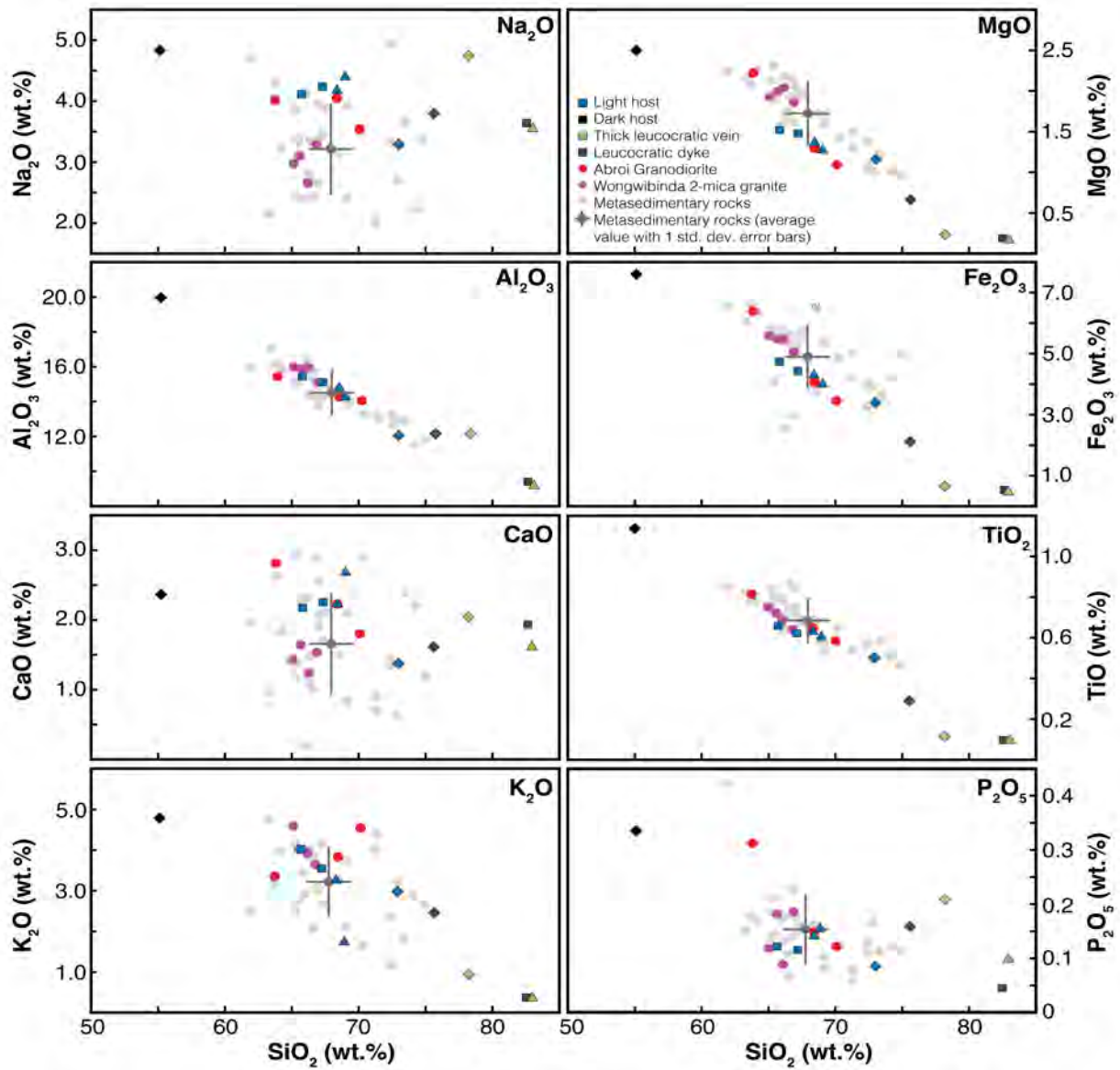


Fig. 17: Whole rock major element oxides (wt.%) plotted against SiO_2 (wt.%). Square (LMC05), triangle (LMC06) and diamond (LMC07) icons are samples from this study. Other data from Kim Jessop (personal communication, 2017) and Henson (2000). Red circles = Abroi Granodiorite. Pink circles = Wongwibinda 2-mica granite. Light grey circles = Wongwibinda Metamorphic Complex metasedimentary rocks (dark grey circle = median value). Square = LMC05, diamond = LMC06, triangle = LMC07.

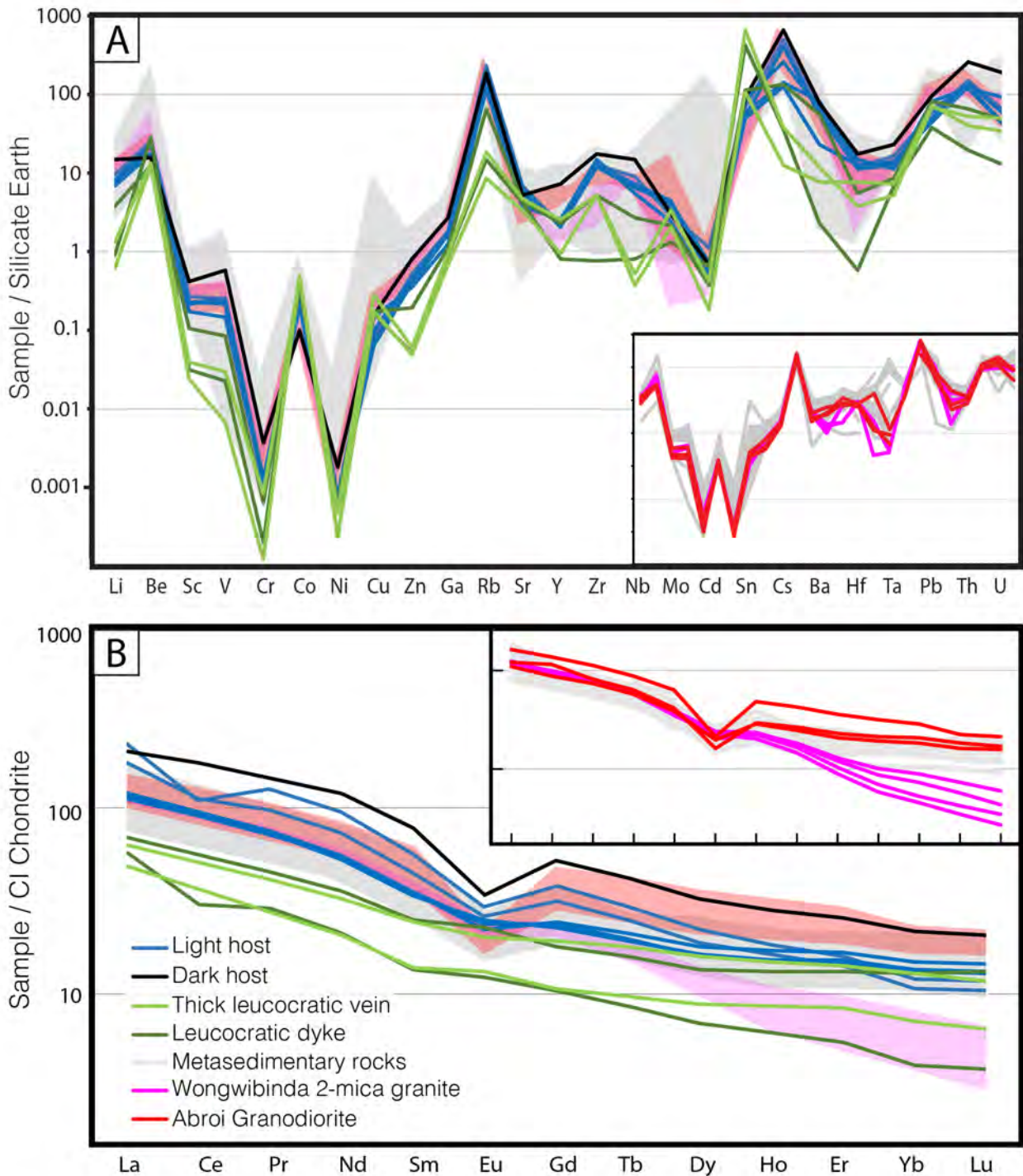


Fig. 18: Whole rock (A) trace element spider plot normalised to silicate earth (McDonough & Sun, 1995) and (B) rare earth element (REE) plot normalised to CI Chondrite (McDonough & Sun, 1995). Black, blue and green lines are samples from this study. Other data from Kim Jessop (personal communication, 2017) and Henson (2000). Red background field and lines (inset) = Abroi Granodiorite. Pink background field and lines (inset) = Wongwibinda 2-mica granite. Light grey background field and lines (inset) = Wongwibinda Metamorphic Complex metasedimentary rocks. Inset shows spread of the data within the background fields.

Major elements

Whole rock major element oxide data (oxide wt.%) is presented in Table 3. Overall, the four types of components analysed (light host, dark host, thick leucocratic veins and leucocratic dykes) are chemically distinct (Fig. 17). SiO_2 is more abundant in leucocratic veins and dykes (75.8-83.2 wt.%) compared to the light host (65.9-73.1 wt.%) and dark host (55.1 wt.%). K_2O content is highest in the dark host (4.8 wt.%) compared to the light host (1.7-4.0 wt.%) and leucocratic veins and dykes (0.3-2.4 wt.%). MgO and Fe_2O_3 contents are much higher in the dark host compared to the light host and leucocratic veins and dykes. Na_2O and CaO contents for all components are similar, only varying by <1.5 wt.%.

Trace and rare earth elements

Whole rock trace and rare earth element data (ppm) is presented in Table 3.

Trace element concentration (ppm) is normalised to silicate Earth values reported by McDonough & Sun (1995) and plotted in Fig. 18. Overall, thick leucocratic veins and dykes are depleted in most elements except Co, Cu and Sn relative to the other migmatite components.

Rare earth element (REE) data (ppm) is normalised to CI Chondrite values reported by McDonough & Sun (1995) and plotted in Fig. 18. The ratio of La/Lu, a proxy for the total REE slope is compared to the ratio of La/Sm, a proxy for the light rare earth element [LREE] slope and Gd/Lu, a proxy for the heavy rare earth element [HREE] slope) (Fig. 19). There is a progression in the REE patterns for the five light-coloured host samples that starts with sample LMC06, with REE patterns closest to the lower-grade metasedimentary rocks of the Wongwibinda Metamorphic Complex. The REE patterns change to progressively steeper LREE and HREE patterns to sample LMC07 and steepening further to sample LMC05. Another striking feature of the data is that the sub-samples of light-coloured host and vein or dyke from a given sample plot closest to each other, indicating veins and dykes share similarly steep REE patterns with their host rocks.

The REE patterns of leucocratic vein and dyke sub-samples from LMC06 share similar steepness to the REE patterns of the Abroi Granodiorite. The REE pattern of the leucocratic vein sub-sample from LMC07 plots at steeper LREE slopes compared to the cluster of metasedimentary rock values and are much steeper than those for the Abroi Granodiorite. The REE pattern of the leucocratic dyke sub-sample from LMC05 has the steepest LREE and HREE slopes of the samples analysed in this study, within range of the light-coloured host components separated from the same sample and the Wongwibinda 2-mica granite is the only samples with steeper patterns. A large negative Eu

anomaly, common to all samples of the Abroi Granodiorite, is also observed in the dark-coloured host component from sample LMC06. Smaller negative Eu anomalies are seen in the metasedimentary rocks and the light-coloured host component samples. The leucocratic veins and dykes, as well as the Wongwibinda 2-mica granite, lack a Eu anomaly. The four Wongwibinda 2-mica granite samples have typical LREE slopes with La/Sm around 3.0, but display a broad range in HREE slopes. This reflects a spatial relationship, with the two samples with the steepest slopes having been sampled from Karuah and Billy's Block, <20km away from the study site. The other two samples of Wongwibinda 2-mica granite were collected on Lynoch station very close to the study site.

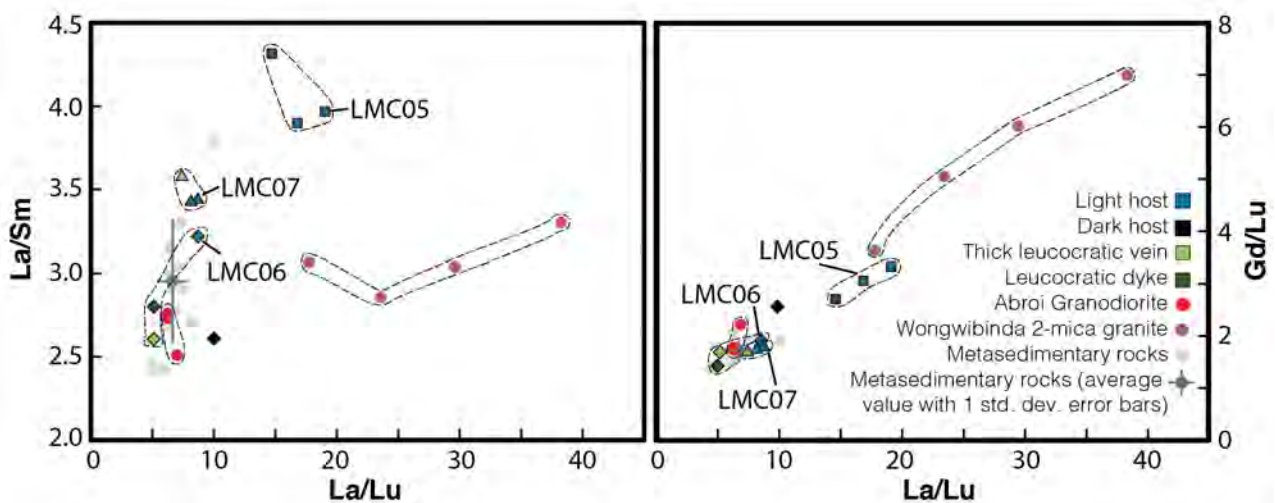


Fig. 19: Whole rock rare earth element (REE) ratio plots showing the total slope of the REE (La/Lu) vs the slope of (A) light rare earth element (LREE; La/Sm) and (B) heavy rare earth element (HREE; Gd/Lu). Red circles = Abroi Granodiorite. Pink circles = Wongwibinda 2-mica granite. Light grey circles = Wongwibinda Metamorphic Complex metasedimentary rocks (dark grey circle = median value). Square = LMC05, diamond = LMC06, triangle = LMC07.

7. Discussion

Two of the main remaining overarching problems in the high-temperature – low-pressure Wongwibinda Metamorphic Complex are the sources of (i) heat and (ii) local plutons. Important to both is identifying the former presence of melt and how it migrated through the local geology. This study focuses on the mechanisms for melt transport within migmatite rocks on Lynoch Station. In this study, two transport mechanisms are identified and discussed below: (i) veining and dyking and (ii) channelled grain-scale melt flow. The presence of volume-loss or collapse structures in the studied migmatites is first discussed, as these indicate that more melt passed through the migmatite rocks than is frozen at the current exposed structural level. A high vol. % of leucocratic material relative to inferred low degrees of in-situ partial melting shows that much of the melt is externally

sourced. Channelled grain-scale melt flux is discussed next to highlight the variable modes of melt migration through the migmatite rocks. This study successfully fulfilled its main aim, to characterise the melt pathways present in the migmatite rocks of the Wongwibinda Metamorphic Complex.

Migmatite classification

The rocks studied on Lynoch station, Wongwibinda Metamorphic Complex are a mix of grey metapsammitic schist and 12.5% lighter leucocratic veins and dykes. A low vol.% of in-situ partial melt (<2%) is inferred for the migmatite rocks, based on calculated maximum metamorphic conditions of 660°C and <3.3 kbar (Craven et al., 2012), and the similarity in major element concentrations of the light host component of migmatite compared to lower grade metasedimentary rocks from elsewhere in the complex (inferred to be the protolith). This suggests that the exposed structural level did not significantly partially melt and it was therefore an insignificant source for local S-type granite petrogenesis. The leucocratic material occurs as veins and dykes that display cross-cutting relationships that are observed across all outcrops in the study area. These veins and dykes are often bordered by biotite rich selvages interpreted to be the result of a reaction between the host schist and the vein or dyke. This and the discrepancy between calculated in-situ partial melting and the amount of leucocratic material observed in the outcrops, rules out interpreting the veins and/or dykes as in-situ or in-source leucosome. Following the terminology used by Sawyer (2008), they are interpreted as leucocratic veins and dykes (Sawyer, 2008), resulting from the injection of an anatectic melt from an external source that is within the zone of anatexis. These observations classify the migmatite rocks as an injection complex and specifically as a vein-structured metatexite migmatite.

Leucocratic veins and collapse structures: Melt migration pathways in the Wongwibinda migmatite

Two types of leucocratic veins are observed to be sub-parallel to the schistosity in the migmatite rocks: (i) quartz+plagioclase (non-granitic), and (ii) quartz+plagioclase+K-feldspar (granitic). At least some granitic veins are interpreted to be older, as fine-grained plagioclase pseudomorphs were observed to partially or completely replace coarse K-feldspar grains (e.g. Fig. 10F) where the quartz+plagioclase veins are in contact with sub-parallel granitic veins. Although the opposite replacement relationship was not observed in the examined samples, it is possible that both types of leucocratic veins were injected sub-parallel to each other throughout the migmatite at the same time. This inference is made because both vein types are cross-cut by leucocratic dykes that are also

granitic (Figs. 5, 13) and is supported by large biotite grains observed at some vein-dyke intersections (Fig. 10E) suggesting a reaction process during injection of melts of slightly different compositions or temperatures. Additionally, some granitic veins are in petrographic continuity with the sub-perpendicular dykes (i.e. the phase distribution and textures observed in the dyke are the same in the vein with no obvious contact where the dyke cut through, e.g. Fig. 13). In summary, there are three types of veins and dykes within the migmatite rocks that are broadly observed to cross cut each other, but are likely to have intruded during the same event: (i) granitic veins are partially replaced by (ii) quartz+plagioclase veins where they intersect, and (iii) younger granitic dykes cut the older veins at a high angle, with some dykes also injecting parallel to the pervasive foliation.

A simple scenario of injection and crystallisation of melt is predicted to form numerous granitic veins and dykes (Brown, 2013), matching the observed quartz+plagioclase+K-feldspar leucocratic vein and dyke component within the migmatite rocks (Table 2). However, quartz+plagioclase leucocratic veins are also common and were interpreted by Farrell (1992) to have formed sub-solidus. These non-granitic veins could be explained by high temperature melting of a mafic source to form tonalite (Hyndman & Foster, 1988), but rather the dominance of S-type plutonism in the local geological context (Binns, 1966; Craven et al., 2012, 2013) argues for a relationship to granitic melt. This inference is supported by the observation of garnet- and/or muscovite-bearing veins and dykes (e.g. Fig. 12), as these minerals are key indicators of S-type granite systems (Clemens & Wall, 1981). Non-granitic veins including tonalite, K-feldspar+quartz, plagioclase+quartz, or nearly pure quartz are common in high-grade rocks (Aranovich et al., 2014) and their interpretation is controversial, with both anatectic (Whitney & Irving, 1994; Morfin et al., 2014) and non-anatectic / sub-solidus (Amit & Eyal, 1976) origins being proposed.

Two options are considered to explain the presence and lack of K-feldspar in different veins and dykes: a) all veins and dykes crystallised from melt or b) only the granitic ones did and the quartz-plagioclase composition crystallised from hot aqueous fluid, not far below the solidus of the rocks.

a) All veins and dykes crystallised from melt:

It is proposed here that subtle differences in temperature of the injecting melt may have controlled whether K-feldspar crystallised in the different leucocratic veins and dykes. Two temperature scenarios are considered in this option, involving injection of granite liquid at approximate temperatures of: (i) 750°C or (ii) 800°C. Regarding granite phase equilibria (Fig. 20, Clemens and

Wall, 1981), it is envisaged that the granitic veins and dykes represent mostly crystallised granite melt that injects with igneous temperatures of about 750°C (orange arrow and point A on Fig. 20). Small proportions of liquid may still escape these systems to lower pressures (end of orange arrow on Fig. 20) or the liquid may completely freeze (and it stops at point A on Fig. 20). In the second scenario, the quartz+plagioclase leucocratic veins form when granite melt injects at igneous temperatures of about 800°C, above the stability of K-feldspar. At this temperature, K-feldspar is yet to crystallise from the liquid (L), while quartz and plagioclase are stable minerals that will crystallise. The extraction of the liquid component before the melt cools below the stability of K-feldspar will leave veins of a quartz+plagioclase composition. In this second scenario, granite melt must escape to lower pressures (end of red arrow on Fig. 20) because if it froze at the exposed level, it would have cooled toward point A on Figure 20 and have crystallised K-feldspar.

b) Non-granitic veins crystallised from hot aqueous fluid:

The second option to consider in the formation of the quartz+plagioclase veins is that they crystallised from a solute-rich aqueous fluid at a temperature below the solidus of the migmatite host component (i.e. less than approximately 650°C). Given that the migmatite rocks in the Wongwibinda Metamorphic Complex are at or near the solidus (Craven et al., 2012), a minor

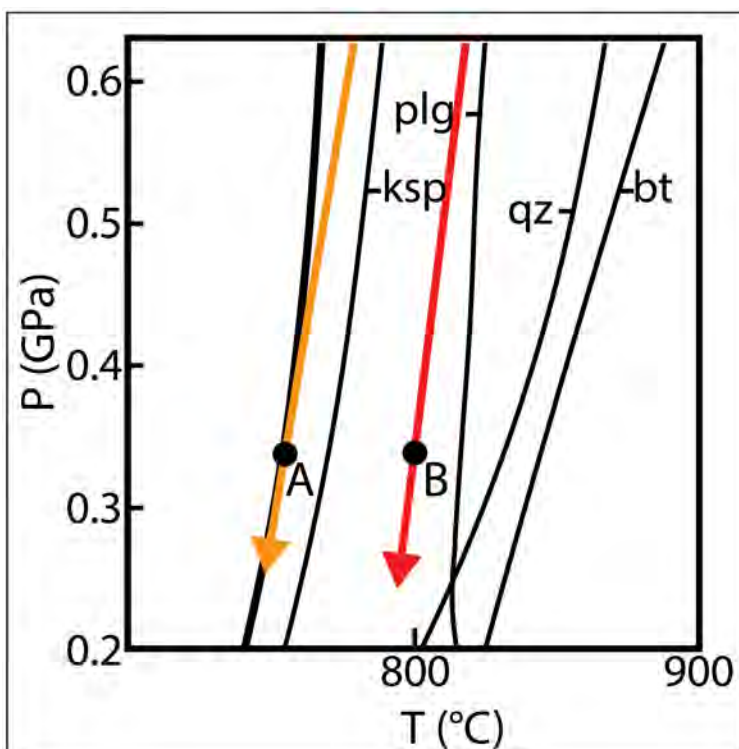


Fig. 20: S-type granite phase equilibrium plot (modified from Clemens & Wall, 1981). Mafic minerals in low abundance (cordierite, orthopyroxene and garnet) are not shown to focus attention on the lower temperature minerals (i.e. K-feldspar, plagioclase, quartz, biotite). Orange and red arrows show two possible P-T paths of migrating melts, above (red arrow) and below (orange arrow) K-feldspar stability.

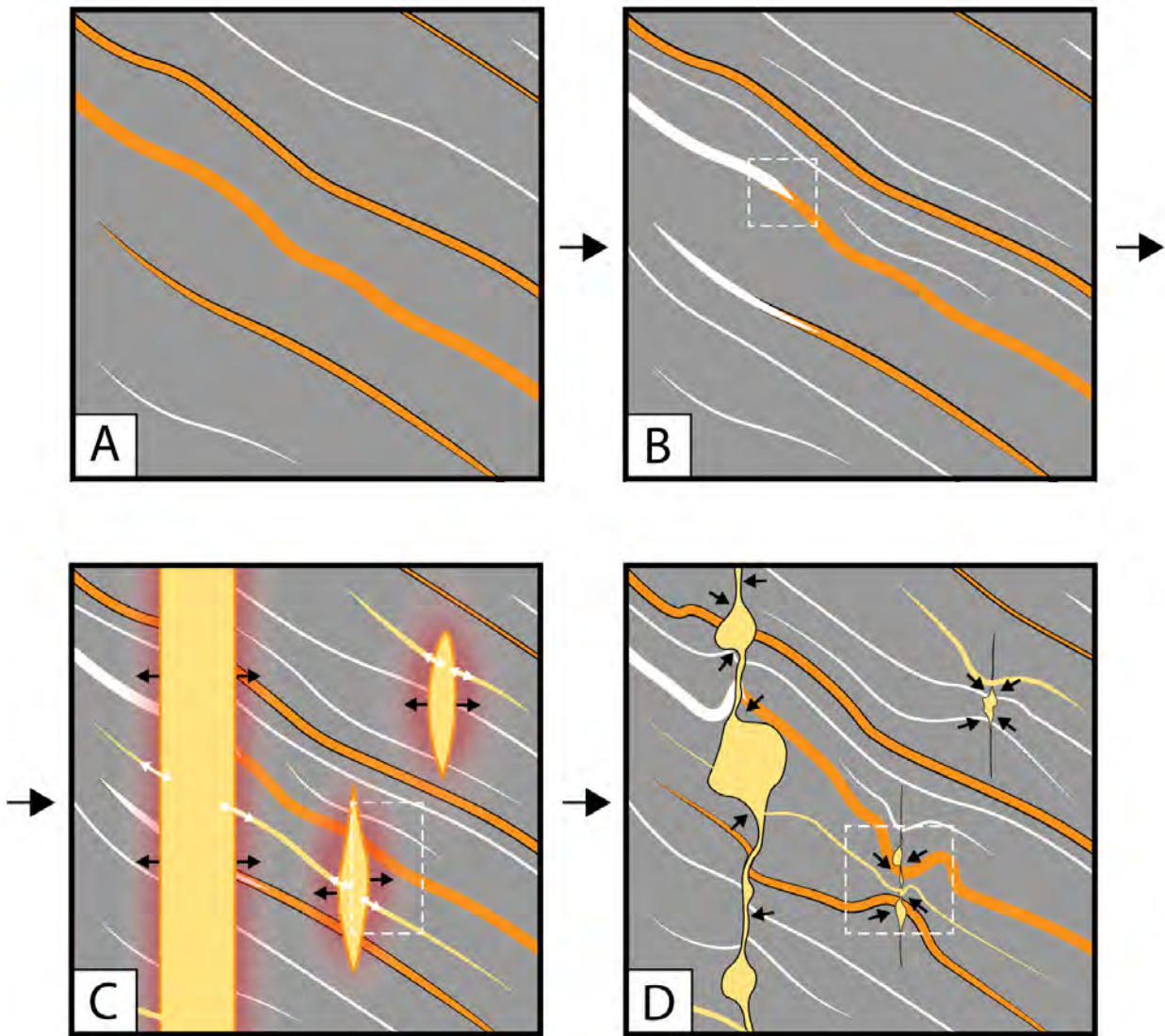


Fig. 21: Schematic component diagrams showing the interpreted sequence of intrusive events leading to collapse structures. (A) Granitic veins are emplaced, some forming biotite rich selvages due to a reaction between the vein composition and the adjacent host. (B) Slightly higher temperature granitic melts inject in the stability field of quartz and plagioclase forming veins that are sub-parallel to the earlier granitic veins. Some quartz-plagioclase veins intersect the pathways of earlier granitic veins, replacing K-feldspar with plagioclase. Note: it is possible that A and B are mutually cross cutting. (C) Intrusion of granitic dykes, cutting the pervasive foliation at a high angle. Some granitic veins related to the dykes, propagate along the pervasive foliation sub-parallel to older veins. (D) Extraction of the remaining liquid leads to trapping of crystal aggregates within the dyke by the contracting walls. This localised warping of the rock creates irregular geometries within the intersecting veins and may pull the nearby veins to a central point to form a pucker or collapse structure.

reduction in temperature would move into the realms of veins formed by crystallisation from solute-rich aqueous fluids (Bons et al., 2012). Quartz+plagioclase vein microstructure is blocky (e.g. Fig.

10A,B), consistent with formation by crystallisation into a fluid filled void (Bons et al., 2012), but not diagnostic of crystallisation from melt or aqueous fluid. Diffuse vein boundaries (e.g. Figs. 8C, 10B, 11A) are indicative of high temperature which is consistent with the near solidus conditions in the migmatite host components. Hasalova et al. (2011) interpret similar diffuse vein boundaries as forming from interaction between melt and the wall rock, possibly supporting the option (a) above.

Collapse structures

Localised irregular, complex patterns of folding and deflection of leucocratic veins adjacent to small cross-cutting leucocratic dykes are observed throughout the migmatite outcrops (e.g. Figs. 3A, 4A-D, 21). These ‘pucker’ patterns ‘pull’ the local vein foliation to a central point (or points) at the intersection with a cross-cutting dyke. The ‘pucker’ structures occur in addition to thicker leucocratic dykes that display variable thickness along strike, showing boudin-like pinch and swell patterns (e.g. Figs. 3B,C, 21D). These geometric patterns are consistent with local deformation to accommodate volume loss during collapse of previously melt filled fractures of variable length (called collapse structures, Bons et al., 2004, Bons et al., 2012). These patterns contrast with shear ‘flanking structures’ that appear similar, but lack the focused deflection of a foliation (Passchier, 2001). If the fracture was extensive (>1m long), melt escape and collapse of this system may form the boudin-like pinch and swell patterns of the leucocratic dykes. Whereas, if the melt-filled fracture was less extensive (<1m long), melt escape and collapse forms the localised ‘pucker’ structures. The large variation in the distribution and geometry of collapse structures between and across the outcrops studied shows that melt migration was variable throughout the system.

Targeted EBSD on the folded quartz+plagioclase leucocratic veins around these collapse structures reveals a lack of pronounced solid-state rotation and deformation (e.g. Fig. 15). The often-diffuse vein and dyke boundaries (e.g. Figs. 8C, 10B, 11A, 15) support the notion that the system was at high temperature, as low temperature veins generally have well defined ‘dry’ boundaries (Bons et al., 2012). The combination of these observations supports the notion that the localised folding of the veins may have been accommodated by melt assisted grain boundary sliding (Simakin & Petford, 2003; Le Roux, 2008) and that melt was present in other components of the migmatite while the leucocratic dykes inflated and then collapsed. The interpretation of the irregular dyke and vein geometries as collapse structures shows that melt has passed through the system and that what is frozen represents a fraction of the total melt that moved through the exposed structural level.

Grain-scale melt flux

Grain-scale porous flow of fluids or melt through rocks involves migration along grain boundaries through interconnected pore networks (Dijkstra et al., 2003). There are two main sub-classifications: (i) diffuse – where pervasive flow of melt occurs throughout much of the rock volume (Dijkstra et al., 2003), and (ii) channelled – where flow of melt is concentrated along narrow pathways such as at lithological contacts or through layers of rock with a higher porosity (Jull et al., 2002). Channelling of an aqueous fluid or melt may occur at multiple scales with channel widths varying from less than a metre to many tens of metres.

Biotite-plagioclase-rich bands, identified in outcrop as “dark-coloured host” (see field and petrography sections), are discordant features that cut previously veined migmatite and are observed in most migmatite outcrops (Figs. 2B,C, 3, 4, 5, 6). The cross cutting nature of these bands (Fig. 5C) is supported by their irregular boundaries and common finger-like pointy extensions (Figs. 5A, 9A). These observations preclude an interpretation of variable protolith composition (i.e. a pelitic bed within the dominantly psammitic schists) or formation of residual melanosome to explain the light- versus dark-coloured host components of the migmatite. Instead, these bands are interpreted to represent channels of grain-scale porous melt flow. In this context, the higher vol. % of biotite (>30 vol. %) and plagioclase (>50 vol.%), and reduction in quartz grain size (<0.1mm) and modal abundance (<4%) in the dark bands (Figs. 9D,E, 14, 22), formed by melt-rock interaction during melt flux (Stuart et al., 2016; Daczko et al., 2016). Additionally, melt-rock interaction formed a high vol. % of apatite in dark host components. Together these observations indicate significant metasomatism of the protolith to the migmatite.

Whole rock geochemical results show a pattern of rare earth element (REE) metasomatism in the migmatite light host components, with a progression from sample LMC06 to LMC07 to LMC05 (e.g. Fig. 19). The light host component of sample LMC06 plots within the cluster of the protolith metasedimentary rocks (Fig. 19). However, this sample contains dark host bands that plot outside of this cluster. While the rocks of Wongwibinda have been fluxed by hydrothermal fluids (Craven et al., 2013), rare earth elements will only be significantly mobilised in the presence of melt (Bickle & McKenzie, 1987; Stuart et al., 2017; Ague, 2017), leading to the interpretation that the dark host bands have channeled melt through the migmatite, causing localised REE metasomatism. The progression of REE metasomatism observed in light host components from samples LMC06 to LMC07 to LMC05 shows a metasomatic progression away from the common protolith pattern

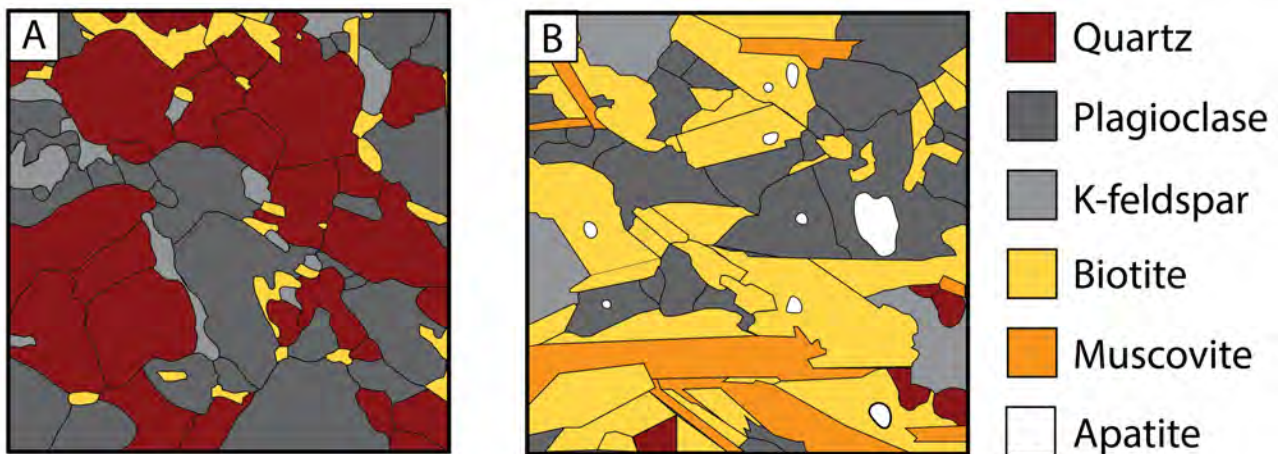


Fig. 22: Schematic microstructure of (A) light host that has had no significant grain-scale porous flow, and (B) host that has experienced channelled porous flow. Muscovite and biotite have a more euhedral grain shape, larger grain size and a shape preferred orientation left to right in (B) compared to (A). Note: relative proportions of quartz (red) and biotite (yellow), the former significantly reduced in grain size and abundance in (B) relative to (A). Also note, significant increase in apatite abundance in (B).

observed in all the lower-grade rocks (Fig. 19). In addition to this, a randomisation of quartz CPO accompanies the increasing metasomatism i.e. the rocks with a marked decrease in quartz content and increase in apatite. This randomisation of quartz CPO is also observed in sample LMC06, but only within the dark-coloured host bands (Fig. 14iii), whereas the CPO is strongly aligned in the adjacent light-coloured host components (Fig. 14i). This suggests that melt has been channelled at variable scales. Sample LMC05 light host component also has a random quartz CPO (Fig. 13i), suggesting that melt fluxed in a broader (>10m wide) channel compared to the smaller dark-coloured host bands in LMC06. Rare randomly distributed quartz grains with a higher internal misorientation (Fig. 13iii) are interpreted to be relict grains that have not been recrystallised during the diffuse grain-scale porous flow. These exhibit systematic internal deformation suggesting solid state deformation by dislocation creep before the melt fluxing event. In addition, the small quartz grains exhibit internal changes in crystallographic orientation, that are non-systematic. In other words, they show in contrast to the large grains, no small circle dispersions in pole figures and no systematic misorientation axes (13ii). These features of the small quartz grains cannot be reconciled with dislocation creep induced orientation changes and are interpreted to be typical for growth from a melt. In this case, local stresses vary and induce non-sytematic accommodation in the growing quartz grain. The dominance of randomly oriented quartz grains is interpreted to result from (re)crystallization in the presence of melt, as supported by abundant cusped K-feldspar grains that

are inferred to represent pseudomorphs of former interstitial melt pockets (Holness, 2008). These occur throughout most of the migmatite host components suggesting that melt migrated by diffuse grain-scale melt flux at a scale that is greater than the outcrop size. This supports the observations of variable REE metasomatism. Taken together, the metasomatism, phase changes, randomisation of quartz CPO and evidence for the pervasive distribution of former melt pockets, it is interpreted that melt fluxed through the Wongwibinda migmatite host components by diffuse grain-scale porous flow.

In summary, channelling of melt flux at different scales from cm- to at least outcrop-scale caused REE metasomatism, phase changes and randomisation of protolith CPO fabrics. This process invokes a second style of melt flux in this study area in addition to veining and dyking.

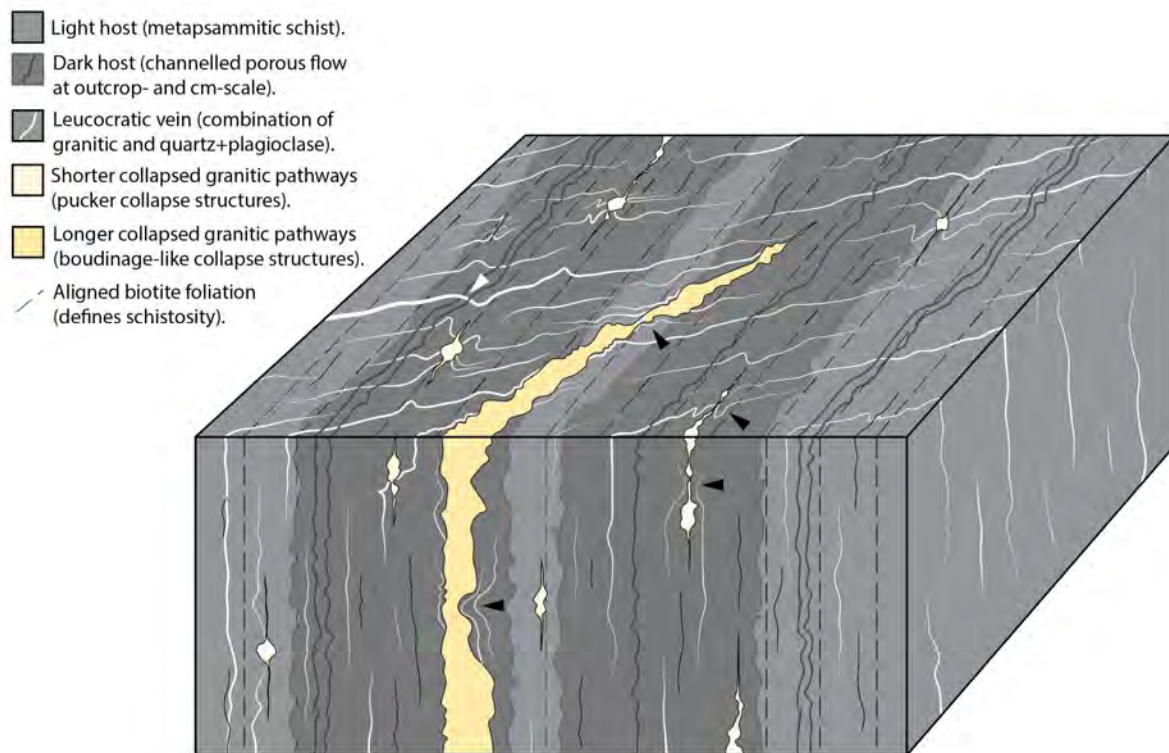


Fig. 23: Schematic block diagram showing the relationships between the components in the migmatite. Two types of flux occur as (i) veining & dyking (White and cream colours. White veins encompass both granitic and non-granitic compositions) and (ii) channelled porous flow at multiple scales (Dark grey thicker bands, darker grey thin lines). Note that collapse structures occur in 3D (i.e. not only on surface plane, black arrows). White arrow shows multiple cross-cutting relationships between veins and cm-scale channelled porous flow, indicating that both events were synchronous.

The Wongwibinda Metamorphic Complex: Open system melt fluxing resulting in the formation of migmatite and localised high heat flux

The migmatite rocks in the Wongwibinda Metamorphic Complex contain thin leucocratic veins and sparser, thicker dykes making up 12.5% of all outcrops studied. This high proportion of leucocratic material contrasts with inferred low degrees of in situ partial melting (~2%) at peak metamorphic conditions of ~660°C and <3.3 kbar (Craven et al., 2013) and is consistent with the fine grain size of the host component of the migmatite rocks. Veins and dykes are interpreted to be leucocratic (i.e. not in-situ leucosome because melt has moved from another source within the zone of anatexis into the migmatite) due to the presence of reaction features such as host metasomatism (Fig. 19) and biotite-rich selvages (Fig. 10E), and the lack of residual rocks (melanosome). Therefore, most of the leucocratic component of the migmatite is inferred to be externally sourced from deeper metasedimentary rocks and to have at least partially accumulated at the exposed structural level, defining the system as open. Injection of melt into rocks near to their solidus conditions commonly results in solidification of the melt and formation of an injection complex (Weinberg & Searle, 1998). This open system variable melt flux would have advected heat into the migmatite rocks. Defined at the beginning of the discussion as vein-structured metatexite migmatite, the rocks studied at Lynoch station have experienced two types of melt flux (Fig. 23) which occurred synchronously, as indicated by a series of cross-cutting relationships between veins and cm-scale channelled grain-scale porous flow (white arrow in Fig. 23). Significant portions of externally derived leucocratic material show that these vein-structured metatexite migmatite rocks formed from the injection of anatectic melt into a metapsammite. The identification of collapse structures and the interpretation that the quartz+plagioclase veins crystallised from melt, both show that some proportion of the injected melt escaped the exposed structural level. These features demonstrate that granitic melt fluxed through the migmatite rocks.

Conclusions

From the above evidence, the migmatite rocks from the Wongwibinda Metamorphic Complex are concluded to be part of an open system, with externally derived melt fluxing through the migmatite in two dominant ways (i) veining and dyking and (ii) channelled porous grain-scale melt flow. With low inferred degrees of in-situ partial melting of the host component of the migmatite, the partial crystallisation of fluxed leucocratic material is proposed to have been the dominant mechanism in the formation of the migmatite rocks, defining these migmatites as an injection complex. The

presence of collapse structures and the evidence for channeled porous grain-scale flow of melt show that some melt moved through the migmatite rocks, supporting a flux hypothesis. This study provides an initial investigation into the formation of an injection migmatite and demonstrates the importance of two types of melt migration. Further analysis could provide insight into how melt moves through the upper crust more broadly and for the development of HTLP metamorphic complexes, both of which are highly debated.

Future directions

This study provides an initial investigation and characterisation of the migmatite rocks in the Wongwibinda Metamorphic Complex. Further work to move towards resolving the anomalously steep thermal field gradient and its potential relationship to melt migration would be to (a) model the thermal impacts of melt flux through the migmatites, and (b) to incorporate isotopic geochemical data to quantify the time integrated melt flux through the system and better constrain the advection of heat via melt migration.

Initial calculations based on the results in this study suggest that a substantial amount of melt could have fluxed through the migmatite rocks. 12.5% of the exposed migmatite comprises leucocratic material. If this component is used as an average value across all migmatites in the complex, then the area of melt that crystallised at this structural level to form the migmatite is calculated at 5.48km². If this area is projected down to 5km below the current exposed level and there are similar proportions of crystallised material, then this results in 5.48km² * 5km depth = 27.38km³ of melt that crystallised in the pathways. This represents the minimum melt volume to have injected the complex, as it is inferred that some melt fluxed and continued to structurally shallower levels.

Local granitoids, the Abroi Granodiorite and Wongwibinda two-mica Granite have surface exposures of 141.58km² and 2.51km² respectively (Kim Jessop, October 2017). If the thickness of these local plutons is taken to be roughly 5km, the total volume of local plutonic material is approximately 720.47km³, 4886.7 times that estimated to have crystallised within the migmatites. This suggests that roughly 3.8% of the melt injected into the migmatite rocks froze to form veins and dykes, while 96.2% fluxed through to build local plutons. While this is a very simple estimate, the relationships shown in this study indicate that quantifying the time integrated flux through zones of migmatite is an avenue of research worth exploring.

Finally, further investigating how much heat could be advected from lower in the crust by melt migration is worthy of further research. This may explain the steep thermal field gradients in HTLP metamorphic complexes such as Wongwibinda and would impact research on other HTLP belts, common in eastern Australia and globally.

References

- AGUE, J. J. 2017. Element mobility during regional metamorphism in crustal and subduction zone environments with a focus on the rare-earth elements (REE). *American Mineralogist*, 102, 1796-1821.
- AMIT, O., EYAL, Y. 1976. The genesis of the Wadi-Magrish migmatites (N-E Sinai). *Contributions to Mineral Petrology*, 59, 95–110.
- ARANOVICH, L. Y., MAKHLUF, A. R., MANNING, C. E., NEWTON, R. C. 2014. Dehydration melting and the relationship between granites and granulites. *Precambrian Research*, 253, 26-37.
- BESTMANN, M., PRIOR, D. J. 2003. Intragranular dynamic recrystallization in naturally deformed calcite marble: diffusion accommodated grain boundary sliding as a result of subgrain rotation recrystallization. *Journal of Structural Geology*, 25, 1597–1613.
- BICKLE, M. J., MCKENZIE, D. 1987. The transport of heat and matter by fluids during metamorphism. *Contributions to Mineralogy and Petrology*, 95, 384–392.
- BINNS, R. A. 1966. Granitic intrusions and regional metamorphic rocks of Permian age from the Wongwibinda district, north-eastern New South Wales. *Journal of the Proceedings, Royal Society of N.S.W.*, 99, 5-36.
- BODORKOS, S., SANDIFORD, M., OLIVER, N. H. S. & CAWOOD, P. A. 2002. High-T, low-P metamorphism in the Palaeoproterozoic Halls Creek Orogen, northern Australia: the middle crustal response to a mantle-related transient thermal pulse. *Journal of Metamorphic Geology*, 20, 217-237.
- BONS, P. D. 1999. Apparent extensional structures due to volume loss. *Proceedings Estonian Academy of Sciences, Geology*, 48, 3-14.
- BONS, P. D., DOUGHERTY-PAGE, J. & ELBURG, M. A. 2001. Stepwise accumulation and ascent of magmas. *Journal of Metamorphic Geology*, 19, 627-633.
- BONS, P. D., DRUGUET, E., HAMANN, I., CARRERAS, J. & PASSCHIER, C. W. 2004. Apparent boudinage in dykes. *Journal of Structural Geology*, 26, 625-636.
- BONS, P. D., DRUGUET, E., CASTANO, L. & ELBURG, M. A. 2008. Finding what is now not there anymore: Recognising missing fluid and magma volumes. *Geology*, 36, 851-854.
- BONS, P. D., BECKER, J. K., ELBURG, M. A. & URTSON, K. 2009. Granite formation: Stepwise accumulation of melt or connected networks? *Earth and Environmental Science Transactions of the Royal Society of Edinburgh*, 100, 105-115.
- BROWN, M. 1973. The Definition of Metatexis, Diatexis and Migmatite. *Proceedings of the Geologists' Association*, 84, 371-382.
- BROWN, M. 2013. Granite: From genesis to emplacement. *GSA Bulletin*, 125, 7/8, 1079-1113.
- CARRERAS, J. & DRUGUET, E. 1994. Structural zonation as a result of inhomogeneous non-coaxial deformation and its control on syntectonic intrusions: an example from the Cap de Creus area, eastern-Pyrenees. *Journal of Structural Geology*, 16, 1525-1534.
- CLEMENS, J. D., WALL, V. J. 1981. Origin and crystallisation of some peraluminous (S-type_ granitic magmas. *Canadian Mineralogist*, 19, 111-131.
- CRAVEN, S. J., DACZKO, N. R. & HALPIN, J. A. 2012. Thermal gradient and timing of high-T–low-P metamorphism in the Wongwibinda Metamorphic Complex, southern New England Orogen, Australia. *Journal of Metamorphic Geology*, 30, 3-20.

- CRAVEN, S. J., DACZKO, N. R. & HALPIN, J. A. 2013. High-T–low-P thermal anomalies superposed on biotite-grade rocks, Wongwibinda Metamorphic Complex, southern New England Orogen, Australia: heat advection by aqueous fluid? *Australian Journal of Earth Sciences*, 60, 1-15.
- DACZKO, N. R., PIAZOLO, S., MEEK, U., STUART, C. A., ELLIOTT, V. 2016. Hornblendite delineates zones of mass transfer through the lower crust. *Scientific Reports*. 6, 31369, 1-6.
- DANIS, C. R., DACZKO, N. R., LACKIE, M. A. & CRAVEN, S. J. 2010. Retrograde metamorphism of the Wongwibinda Complex, New England Fold Belt and the implications of 2.5D subsurface geophysical structure for the metamorphic history. *Australian Journal of Earth Sciences*, 57, 357-375.
- DIJKSTRA, A. H., BARTH, M. G., DRURY, M. R., MANSON, P. R. D., VISSERS, L. M. 2003. Diffuse porous melt flow and melt-rock reaction in the mantle lithosphere at a slow-spreading ridge: A structural petrology and LA-ICP-MS study of the Othris Peridotite Massif (Greece). *Geochemistry, Geophysics, Geosystems*. 4, 8, 1-24.
- FARRELL, T. R. 1992. Deformation, Metamorphism and Migmatite Genesis in the Wongwibinda Metamorphic Complex. *Unpublished PhD thesis, University of Newcastle, Australia*.
- FLEMING, P. D. & WHITE, A. J. R. 1984. Relationships between deformation and partial melting in the Palmer migmatites, South Australia. *Australian Journal of Earth Sciences*, 31, 351-360.
- FLOOD, R. H. & VERNON, R. H. 1978. The Cooma Granodiorite, Australia: An example of in situ crustal anatexis. *Geology*, 6, 81-84.
- GODFREY, J.D. 1954. The Origin of Ptygmatic Structures. *The Journal of Geology*. 64, 4, 375-387.
- GRIFFIN, W. L., POWELL, W. J., PEARSON, N. J. & O'REILLY, S. Y. 2008. GLITTER: data reduction software for laser ablation ICP-MS. In: Sylvester, P. (ed.) *Laser Ablation- ICP-MS in the Earth Sciences*, Mineralogical Association of Canada Short Course Series, 204-207.
- GUERNINA, S. & SAWYER, E. W. 2003. Large-scale melt-depletion in granulite terranes: an example from the Archean Ashuanipi Subprovince of Quebec. *Journal of Metamorphic Geology*, 21, 181-201.
- HAND, M. & DIRKS, P. H. G. M. 1992. The influence of deformation on the formation of axial-planar leucosomes and the segregation of small melt bodies within the migmatitic Napperby Gneiss, central Australia. *Journal of Structural Geology*, 14, 591-604.
- HASALOVA, P., SCHULMANN, K., LEXA, O., STIPSKA, P., HROUDA, F., ULRICH, S., HALODA, J. & TYCOVA, P. 2008. Origin of migmatites by deformation-enhanced melt infiltration of orthogneiss: a new model based on quantitative microstructural analysis. *Journal of Metamorphic Geology*, 26, 29-53.
- HASALOVA, P., WEINBERG, R. F., MACRAE, C. 2011. Microstructural evidence for magma confluence and reusage of magma pathways: implications for magma hybridization, Karakoram Shear Zone in NW India. *Journal of Metamorphic Geology*. 29, 875–900.
- HENSON, A. 2000. A geochemical study of the metasediments of the Wongwibinda Metamorphic Complex, southern NEFB, Australia. *Unpublished Honours thesis, Macquarie University*.
- HOLNESS, M. B., SAWYER, E. W. 2008. On the Pseudomorphing of Melt-filled Pores During the Crystallization of Migmatites. *Journal of Petrology*. 49, 7, 1343-1363.
- HUERTA, A. D., ROYDEN, L. H. & HODGES, K. V. 1998. The thermal structure of collisional orogens as a response to accretion, erosion, and radiogenic heating. *Journal of Geophysical Research*, 103, 15,287-15,302.
- HUGHES, C. J. 1970. The significance of biotite selvages in migmatites. *Geological Magazine*, 107, 21-24.

- HYNDMAN, D. W., FOSTER, D. A. 1988. The Role of Tonalites and Mafic Dikes in the Generation of the Idaho Batholith. *The Journal of Geology*. 96, 1, 31-46.
- JENKINS, R. B., LANDENBERGER, B. & COLLINS, W. J. 2002. Late Palaeozoic retreating and advancing subduction boundary in the New England Fold Belt, New South Wales. *Australian Journal of Earth Sciences*, 49, 467-489.
- JOHANNES, W. 1988. What controls partial melting in migmatites? *Journal of Metamorphic Geology*, 6, 451-465.
- JULL, M., KELEMEN, P. B., SIMS, K. 2002. Consequences of diffuse and channelled porous melt migration on uranium series disequilibria. *Geochimica et Cosmochimica Acta*. 66, 23, 4133-4148.
- KALT, A., CORFU, F., WIJBRANS, J. R. 2000. Time calibration of a P–T path from a Variscan high-temperature low-pressure metamorphic complex (Bayerische Wald, Germany), and the detection of inherited monazite. *Contributions to Mineralogy and Petrology*. 138, 2, 143-163.
- KEMP, A. I. S., SHIMURA, T., HAWKESWORTH, C. J. 2007. Linking granulites, silicic magmatism, and crustal growth in arcs: Ion microprobe (zircon) U-Pb ages from the Hidaka metamorphic belt, Japan. *Geology*. 35, 9, 807-810.
- KISTERS, A.F.M., WARD, R.A., ANTHONISSEN, C.J., VIETZE, M.E. 2009. Melt segregation and far-field melt transfer in the mid-crust. *Journal of the Geological Society*, 166, 905-918.
- KORSCH, R. J. 1978. Stratigraphic and igneous units in the Rockvale-Coffs Harbour region, northern New South Wales. *Journal and Proceedings of the Royal Society of New South Wales*, 111, 13-17.
- KORSCH, R. J. 1981. Structural geology of the Rockvale Block, northern New South Wales. *Journal of the Geological Society of Australia*, 28, 51-70.
- KREIGSMAN, L.M. 2001. Quantitative field methods for estimating melt production and melt loss. *Physics and Chemistry of the Earth, Part A*. 26, 247-253.
- LANGMUIR, C. H., KLEIN, E. M., PLANK, T. 1993. Petrological Systematics of Mid-Ocean Ridge Basalts: Constraints on Melt Generation Beneath Ocean Ridges, in *Mantle flow and melt generation at mid-ocean ridges*, *Geophys. Monograph* 71. p183-280.
- LEITCH, E. C. 1974. The geological development of the southern part of the New England Fold Belt. *Journal of Geological Society of Australia*, 21, 133-156.
- LE ROUX, V. 2008. Melt-rock interactions and melt-assisted deformation in the Lherz peridotite, with implications for the structural, chemical and isotopic evolution of the lithospheric mantle. *Geochemistry*. University Montpellier 2. English.
- LUX, D. R., DEYOREO, J. J., GULDOTTI, C. V. & DECKER, E. R. 1986. Role of plutonism in low-pressure metamorphic belt formation. *Nature*, 323, 794-797.
- MCDONOUGH, W. F., and SUN, S. 1995. The composition of the Earth. *Chemical Geology*. 120, 223 – 253.
- MORFIN, S., SAWYER, E. W., BANDYAYERA, D. 2013. Large volumes of anatectic melt retained in granulite facies migmatites: An injection complex in northern Quebec. *Lithos*. 168-169, 200-218.
- NORMAN, M. D., PEARSON, N.J., SHARMA, A and GRIFFIN, W.L., 1996. Quantitative analysis of trace elements in geological materials by laser ablation ICPMS: instrumental operating conditions and calibration values of NIST glasses. *Geostandards Newsletter*, 20, 247-253.
- PASSCHIER, C. W. 2001. Flanking structures. *Journal of Structural Geology*. 23, 951-962.
- PRIOR, D. J., WHEELER, J., PERUZZO, L., SPIESS, R., & STOREY, C. 2002. Some garnet microstructures: an illustration of the potential of orientation maps and misorientation analysis in microstructural studies. *Journal of Structural Geology*. 24, 999–1011.

- RICHARDS, S. W., COLLINS, W. J. 2002. The Cooma Metamorphic Complex, a low-P, high-T (LPHT) regional aureole beneath the Murrumbidgee Batholith. *Journal of Metamorphic Petrology*, 20, 1, 119-134.
- SANDIFORD, M. & HAND, M. 1998. Australian Proterozoic high-temperature, low-pressure metamorphism in the conductive limit. In: TRELOAR, P. J. & O'BRIEN, P. J. (eds) *What Drives Metamorphism and Metamorphic Reactions?* Geological Society, London, *Special Publications*, 138, 109-120.
- SANDIFORD, M., HAND, M. & MCLAREN, S. 1998. High geothermal gradient metamorphism during thermal subsidence. *Earth and Planetary Science Letters*, 163, 149-165.
- SAWYER, E. W. 1998. Formation and Evolution of Granite Magmas During Crustal Reworking: The Significance of Diatexites. *Journal of Petrology*, 39, 1147-1167.
- SAWYER, E. W. 2008. *Atlas of Migmatites*, NRC Research Press.
- SIMAKIN, A. G., PETFORD, N. 2003. Melt redistribution during the bending of a porous, partially melted layer. *Geophysical Research Letters*, 30, 11, 1-4.
- STUART, C. A., DACZKO, N. R. and PIAZOLO, S. 2017. Local partial melting of the lower crust triggered by hydration through melt–rock interaction: an example from Fiordland, New Zealand. *J. Metamorph. Geol.* 35, 213–230.
- SWANSON, S. 1997. Relation of nucleation and crystal-growth rate to the development of granitic textures. *Am Mineral* 62:966–978
- VERNON, R. H. 1982. Isobaric cooling of two regional metamorphic complexes related to igneous intrusions in southeastern Australia. *Geology*, 10, 76-81.
- VERNON, R. H. & COLLINS, W. J. 1988. Igneous microstructures in migmatites. *Geology*, 16, 1126-1129.
- VERNON, R. H. 2011. Microstructures of melt-bearing regional metamorphic rocks. *Memoir of the Geological Society of America*, 207. 1-12.
- WEINBERG, R. F., and SEARLE, M. P. 1998. The Pangong Injection Complex, Indian Karakoram: A case of pervasive granite flow through hot viscous crust. London, *Journal of the Geological Society*. 155, 883–891.
- WEINBERG, R. F., MARK, G. 2008. Magma migration, folding, and disaggregation of migmatites in the Karakoram Shear Zone, Ladakh, NW India. *GSA Bulletin*. 120, 7/8, 994-1009.
- WEINBERG, R. F., HASALOVA, P. 2015. Water-fluxed melting of the continental crust: A review. *Lithos*. 212-215, 158-188.
- WHITNEY, D. L., IRVING, A. J. 1994. Origin of K-poor leucosomes in a metasedimentary migmatite complex by ultrametamorphism, synmetamorphic magmatism and subsolidus processes. *Lithos*. 32, 173–192.
- WILSON, G. 1952. Ptygmatic Structures and their Formation. *Geological Magazine*. 89, 1, 1-21.
- WINSLOW, D. M., ZEITLER, P. K., CHAMBERLAIN, C. P. & HOLLISTER, L. S. 1994. Direct evidence for steep geotherm under conditions of rapid denudation, Western Himalaya, Pakistan. *Geology*, 22, 1075-1078.
- WHITE, A. J. R. & CHAPPELL, B. W. 1977. Ultrametamorphism and Granitoid Genesis. *Tectonophysics*, 43, 7-22.

Appendix 1 (1/2): Comparison whole-rock geochemical data. Metased = metasedimentary rocks, Abroi GD = Abroi Granodiorite, WG = Wongwibinda two-mica Granite

Rock type	Metased																
Owner	Henson	Jessop	Jessop	Jessop	Jessop	Jessop											
Sample	AH11A	AH11C	AH13B	AH20B	AH20C	AH20A	AH20qA	AH20B	AH20E	AH03G	AH043	AH045	WJ1405	WJ1320	WJ1501	WJ1636	WJ1638
SiO₂	72.46	66.39	66.01	66.98	66.79	74.28	69.23	65.48	74.97	68.59	70.35	67.51	63.79	67.03	65.36	66.18	67.37
TiO₂	0.57	0.63	0.69	0.83	0.85	0.50	0.52	0.76	0.46	0.68	0.64	0.67	0.77	0.72	0.83	0.78	0.68
Al₂O₃	13.23	14.47	16.32	13.68	14.12	11.48	14.02	15.07	11.83	14.70	13.33	14.96	16.14	14.84	14.97	14.37	14.30
Fe₂O₃	2.98	2.34	5.00	4.62	2.74	3.85	4.96	3.77	4.59	3.45	4.47	5.29	6.61	5.06	5.71	5.71	5.44
MnO	0.06	0.07	0.04	0.11	0.10	0.06	0.06	0.09	0.06	0.07	0.07	0.08	0.29	0.20	0.23	0.24	0.24
MgO	1.06	1.72	1.58	2.05	2.14	0.99	1.58	1.90	0.94	1.71	1.42	1.94	2.08	1.62	2.30	2.16	1.98
CaO	1.34	1.46	0.21	2.53	2.88	2.19	2.09	2.26	1.17	1.50	2.88	2.10	2.61	2.05	2.92	2.30	1.68
Na₂O	4.90	3.35	2.41	2.67	3.33	2.22	3.92	3.38	3.37	3.13	3.47	3.86	4.29	3.35	3.83	4.14	3.45
K₂O	1.19	3.99	3.44	3.07	2.08	2.88	2.09	2.71	2.63	3.22	1.64	2.68	3.17	3.04	2.45	2.89	4.14
P₂O₅	0.11	0.13	0.17	0.22	0.23	0.12	0.10	0.21	0.11	0.16	0.12	0.16	0.18	0.14	0.18	0.18	0.15
LOI	0.00	0.00	0.00	0.00	0.00	0.00	0.00	0.00	0.00	0.00	0.00	0.00	1.20	1.03	1.20	1.05	0.94
Total	99.86	97.51	100.61	99.17	97.68	100.64	100.12	98.27	101.94	98.89	100.22	100.68	101.00	98.96	99.87	99.90	100.30
As	0.00	0.00	0.00	0.00	0.00	0.00	0.00	0.00	0.00	0.00	0.00	0.00	13.00	5.00	0.00	7.00	4.00
Ba	352.14	507.38	629.28	661.42	546.09	366.90	326.72	556.15	314.16	591.41	240.57	574.89	409.00	498.00	265.00	440.65	694.00
Be	1.90	1.43	2.26	1.56	1.88	1.69	1.98	2.50	1.31	2.08	1.83	2.37	0.00	0.00	0.00	2.23	0.00
Bi	0.00	0.00	0.00	0.00	0.00	0.00	0.00	0.00	0.00	0.00	0.00	0.00	2.00	2.00	1.00	2.00	1.00
Cd	0.11	0.17	0.33	0.18	0.11	0.18	0.13	0.16	0.46	0.13	0.07	0.20	-3.00	-1.00	0.00	0.03	10.00
Ce	53.49	56.98	65.45	47.86	47.75	41.18	57.50	64.74	54.96	65.06	48.17	42.20	74.00	68.00	46.00	45.50	53.00
Co	24.59	25.27	11.50	43.00	30.45	74.07	37.53	44.67	59.27	36.78	48.15	33.26	29.00	16.00	20.00	39.77	26.00
Cr	13.06	27.63	24.71	32.63	37.78	29.59	24.54	39.03	22.30	30.56	26.08	24.73	47.00	39.00	32.00	46.63	39.00
Cs	1.56	4.90	9.00	6.30	4.67	5.57	6.04	8.50	3.14	12.56	4.17	9.25	-1.00	1.00	0.00	7.07	2.00
Cu	7.69	17.36	11.73	11.31	10.10	106.10	22.55	58.34	6.94	21.00	24.98	18.78	8.00	17.00	11.00	35.26	11.00
Dy	4.55	5.00	5.16	5.64	5.69	3.96	4.77	6.40	4.15	4.76	3.76	4.88	0.00	0.00	0.00	5.13	0.00
Er	2.78	3.04	2.87	3.31	3.45	2.41	2.76	3.43	2.40	3.04	2.45	3.14	0.00	0.00	0.00	3.13	0.00
Eu	1.20	1.34	1.46	1.51	1.49	1.13	1.33	1.57	1.13	1.51	1.18	1.25	0.00	0.00	0.00	1.32	0.00
Ga	6.63	12.14	9.40	14.86	15.13	11.61	11.50	18.18	11.06	16.49	13.29	16.60	20.00	16.00	14.00	16.66	17.00
Gd	4.89	5.69	6.59	5.45	6.61	4.18	5.60	7.76	5.09	6.45	4.60	4.80	0.00	0.00	0.00	5.33	0.00
Ge	0.00	0.00	0.00	0.00	0.00	0.00	0.00	0.00	0.00	0.00	0.00	0.00	1.00	2.00	2.00	2.00	2.00
Hf	3.76	3.94	4.27	4.04	4.13	3.54	4.24	4.17	3.75	4.44	3.58	4.69	4.00	6.00	4.00	4.04	2.00
Ho	0.96	1.05	1.01	1.17	1.21	0.84	0.97	1.19	0.85	1.07	0.86	1.24	0.00	0.00	0.00	1.07	0.00
La	24.43	29.93	28.93	22.90	23.18	19.00	26.36	29.46	32.92	30.54	23.60	19.66	39.00	34.00	27.00	21.12	30.00
Li	23.62	32.69	27.17	11.05	12.39	10.47	24.52	11.73	10.49	11.50	10.25	11.59	0.00	0.00	0.00	21.08	0.00
Lu	0.38	0.42	0.47	0.46	0.46	0.32	0.38	0.47	0.33	0.42	0.33	0.44	0.00	0.00	0.00	0.44	0.00
Mo	0.27	0.27	0.57	0.17	0.14	0.32	0.28	0.31	0.12	0.29	0.27	0.38	1.00	1.00	0.00	0.46	2.00
Nb	7.99	7.63	10.81	6.84	5.84	4.04	6.26	7.49	4.94	8.32	5.82	7.92	7.00	7.00	6.00	8.22	7.00
Nd	22.52	27.85	31.90	24.88	25.81	20.11	28.02	31.43	28.91	31.66	23.67	20.77	32.00	34.00	20.00	23.52	24.00
Ni	4.67	12.29	7.24	17.52	17.28	9.99	10.46	21.15	7.07	16.92	11.51	44.66	15.00	15.00	11.00	21.55	16.00
Pb	16.04	16.40	13.97	12.62	12.16	8.26	16.36	12.39	14.97	14.47	12.81	11.44	13.00	14.00	14.00	13.90	16.00
Pr	5.86	7.15	8.09	6.34	6.46	5.13	7.24	8.06	7.53	8.21	6.20	5.36	0.00	0.00	0.00	5.99	0.00
Rb	39.20	136.72	137.22	97.50	62.22	108.79	68.86	98.09	89.48	101.10	55.60	94.62	96.00	105.00	69.00	78.97	132.00
Sb	0.83	0.58	1.15	0.71	0.51	2.48	0.96	1.30	1.42	1.19	1.40	0.87	-5.00	-4.00	0.00	-2.00	-7.00
Sc	6.64	11.14	10.87	16.74	17.64	9.33	10.13	15.68	8.49	13.81	11.82	13.65	20.00	14.00	12.00	17.77	11.00
Se	0.00	0.00	0.00	0.00	0.00	0.00	0.00	0.00	0.00	0.00	0.00	0.00	-1.00	0.00	0.00	0.00	-1.00
Sm	4.85	5.71	6.74	5.85	6.00	4.35	5.94	6.71	5.45	6.55	4.87	4.74	9.00	6.00	0.00	5.31	-9.00
Sn	2.62	3.02	4.14	2.88	2.37	2.28	2.22	2.73	1.54	2.95	1.32	3.02	0.00	0.00	0.00	5.00	2.00
Sr	272.47	174.81	153.39	270.95	253.68	225.39	251.31	216.38	203.40	188.18	256.03	203.72	284.00	171.00	188.00	243.88	204.00
Ta	1.69	0.92	0.78	1.05	0.64	0.88	1.15	1.10	1.15	0.95	0.88	0.95	0.00	1.00	0.00	0.58	-2.00
Tb	0.76	0.85	0.94	0.93	0.96	0.67	0.84	0.99	0.74	0.92	0.71	0.76	0.00	0.00	0.00	0.85	0.00
Th	8.84	9.81	12.06	6.88	6.03	5.27	9.99	7.56	6.61	8.59	6.06	7.26	13.00	11.00	8.00	7.83	13.00
U	1.98	2.30	2.72	1.44	1.32	1.24	2.22	1.71	1.35	1.89	1.41	1.67	3.00	3.00	1.00	1.75	4.00
V	30.81	58.53	55.56	97.41	93.47	45.88	50.39	90.05	39.12	69.84	61.89	70.17	127.00	110.00	107.00	102.33	100.00
Y	32.37	27.65	31.83	32.75	32.29	23.83	24.13	32.64	24.74	29.80	24.33	30.00	36.00	34.00	28.00	33.94	29.00
Yb	2.58	2.84	2.89	3.10	3.16	2.18	2.55	3.19	2.23	2.82	2.21	2.92	2.00	4.00	1.00	2.94	3.00
Zn	27.37	54.62	71.72	75.40	76.69	43.96	61.76	83.56	56.09	82.72	65.65	84.98	101.00	88.00	70.00	84.68	85.00
Zr	152.82	131.15	176.45	156.94	158.17	125.36	137.87	160.99	138.22	171.12	144.14	191.32	194.00	188.00	184.00	160.24	180.00

Appendix 1 (2/2): Comparison whole-rock geochemical data. Metased = metasedimentary rocks, Abroi GD = Abroi Granodiorite, WG = Wongwibinda two-mica Granite

Rock type	Metased	Abroi GD	Abroi GD	Abroi GD	WG	WG	WG	WG													
Owner	Jessop	Jessop	Jessop	Jessop	Jessop	Jessop	Jessop														
Sample	WJ1314	WJ1383	WJ1470	WJ1640	WJ1347	WJ1348	WJ1389	WJ1643	WJ1364	WJ1648	WJ1363	WJ1387	WJ1334	WJ1559	WJ1541	WJ1567	WJ1559	WJ1604	WJ1651	WJ1652	
SiO2	66.48	72.95	66.66	67.07	61.91	65.29	71.37	64.25	66.30	65.54	71.43	72.46	69.21	66.93	68.49	63.86	66.93	66.25	65.14	65.72	
TiO2	0.70	0.49	0.72	0.74	0.84	0.74	0.53	0.77	0.77	0.78	0.53	0.56	0.57	0.63	0.64	0.81	0.63	0.67	0.74	0.71	
Al2O3	15.19	12.84	15.71	14.84	15.98	15.22	13.17	15.82	15.75	15.91	12.95	12.66	13.85	15.12	14.21	15.36	15.12	15.91	15.99	15.81	
Fe2O3	5.32	3.97	5.65	5.25	6.55	5.82	5.04	6.37	5.55	5.72	4.18	4.01	5.41	5.05	4.07	6.41	5.05	5.44	5.60	5.44	
MnO	0.24	0.44	0.22	0.22	0.31	0.18	0.56	0.27	0.16	0.17	0.85	0.18	0.51	0.23	0.21	0.34	0.23	0.23	0.21	0.21	
MgO	1.74	0.99	1.91	1.90	2.23	2.12	1.50	2.26	1.67	1.89	1.29	1.38	1.71	1.86	1.29	2.22	1.86	2.03	1.93	1.98	
CaO	1.08	0.63	0.98	1.91	1.95	1.16	0.88	1.81	1.17	1.36	0.70	1.42	0.84	1.52	2.20	2.80	1.52	1.23	1.41	1.64	
Na2O	2.76	2.70	2.43	3.93	4.65	2.40	1.99	3.20	2.83	3.27	2.06	3.30	2.40	3.28	4.03	4.01	3.28	2.67	2.96	3.10	
K2O	3.81	3.20	3.80	3.01	2.47	4.12	3.97	3.96	3.89	4.00	4.39	2.36	3.70	3.63	3.82	3.33	3.63	3.92	4.57	4.02	
P2O5	0.10	0.16	0.06	0.17	0.43	0.14	0.07	0.17	0.13	0.14	0.05	0.13	0.08	0.19	0.15	0.31	0.19	0.09	0.12	0.18	
LOI	1.65	1.22	2.33	1.59	2.71	1.73	1.15	1.20	2.18	1.32	1.46	1.52	1.10	1.37	0.79	0.93	1.37	1.89	1.32	1.32	
Total	98.99	99.35	100.37	100.52	99.85	98.85	99.93	100.00	100.31	100.06	99.43	99.88	99.65	99.06	99.15	99.41	99.06	99.55	99.90	100.02	
As	4.50	1.00	0.00	5.00	13.00	2.00	6.00	5.00	8.10	7.00	5.00	14.00	-0.50	5.00	0.00	6.00	5.00	0.00	1.00	3.00	
Ba	772.00	308.00	560.00	501.00	412.00	498.00	596.00	696.73	620.90	564.00	879.00	867.00	432.88	605.42	508.80	393.31	605.42	725.67	906.58	661.71	
Be	0.00	0.00	0.00	0.00	0.00	0.00	0.00	2.62	0.00	0.00	0.00	0.00	3.30	3.74	3.18	3.17	3.74	5.73	2.72	3.38	
Bi	0.50	2.00	2.00	2.00	0.00	1.00	2.00	2.00	1.00	3.00	2.00	1.00	0.50	3.00	3.00	2.00	3.00	2.00	3.00	3.00	
Cd	-1.00	1.00	4.00	6.00	4.00	3.00	-2.00	0.01	-3.00	7.00	-3.00	3.00	0.00	0.04	0.09	0.13	0.04	0.03	0.00	0.00	
Ce	68.00	44.00	58.00	51.00	58.00	52.00	51.00	52.49	53.00	43.00	45.00	40.00	48.98	58.08	54.03	81.08	58.08	58.07	60.14	59.48	
Co	13.50	38.00	17.00	24.00	16.00	22.00	28.00	26.40	24.65	29.00	29.00	20.00	48.12	51.47	44.60	37.53	51.47	40.42	46.49	40.18	
Cr	62.00	43.00	35.00	43.00	47.00	66.00	38.00	46.67	59.80	40.00	33.00	48.00	36.35	35.34	22.25	42.86	35.34	43.20	48.89	53.50	
Cs	4.00	-7.00	6.00	-3.00	-2.00	12.00	8.00	10.30	0.00	11.00	2.00	3.00	11.67	12.54	5.73	11.90	12.54	9.62	10.50	11.02	
Cu	22.50	15.00	25.00	14.00	14.00	30.00	42.00	21.14	36.65	5.00	20.00	20.00	277.12	10.60	19.78	25.09	10.60	13.00	20.38	15.83	
Dy	0.00	0.00	0.00	0.00	0.00	0.00	0.00	4.91	0.00	0.00	0.00	0.00	3.19	2.75	5.43	9.05	2.75	2.42	3.19	3.46	
Er	0.00	0.00	0.00	0.00	0.00	0.00	0.00	2.87	0.00	0.00	0.00	0.00	1.82	0.95	3.09	4.80	0.95	0.83	1.30	1.58	
Eu	0.00	0.00	0.00	0.00	0.00	0.00	0.00	1.40	0.00	0.00	0.00	0.00	0.92	1.22	1.17	1.27	1.22	1.33	1.41	1.31	
Ga	19.00	11.00	17.00	16.00	16.00	18.00	15.00	19.86	18.35	17.00	15.00	14.00	18.89	19.71	17.06	19.91	19.71	20.16	21.03	20.28	
Gd	0.00	0.00	0.00	0.00	0.00	0.00	0.00	5.61	0.00	0.00	0.00	0.00	3.93	4.75	5.90	9.79	4.75	4.32	4.96	4.87	
Ge	1.50	3.00	2.00	2.00	0.00	2.00	2.00	2.00	2.00	2.00	3.00	1.00	2.00	3.00	3.00	4.00	3.00	2.00	3.00	2.00	
Hf	3.50	7.00	5.00	6.00	1.00	5.00	2.00	5.02	3.00	3.00	6.00	2.00	3.02	8.00	3.00	4.00	8.00	5.00	1.29	1.23	
Ho	0.00	0.00	0.00	0.00	0.00	0.00	0.00	0.99	0.00	0.00	0.00	0.00	0.62	0.42	1.12	1.81	0.42	0.36	0.52	0.60	
La	42.00	29.00	31.00	33.00	36.00	32.00	26.00	23.73	34.00	25.00	31.00	21.00	20.10	27.91	25.75	37.77	27.91	28.35	27.76	28.62	
Li	0.00	0.00	0.00	0.00	0.00	0.00	0.00	23.89	0.00	0.00	0.00	0.00	25.60	38.36	24.58	36.25	38.36	31.26	33.61	29.47	
Lu	0.00	0.00	0.00	0.00	0.00	0.00	0.00	0.41	0.00	0.00	0.00	0.00	0.25	0.10	0.41	0.55	0.10	0.08	0.12	0.17	
Mo	1.50	1.00	2.00	1.00	2.00	1.00	2.00	0.69	-2.00	1.00	1.00	2.00	3.16	0.27	0.15	1.39	0.27	0.03	0.22	0.24	
Nb	7.00	6.00	9.00	6.00	7.00	9.00	7.00	10.43	6.30	8.00	7.00	6.00	9.69	10.98	8.02	10.18	10.98	11.15	11.13	10.51	
Nd	28.00	17.00	21.00	27.00	36.00	20.00	14.00	27.54	21.00	27.00	16.00	15.00	21.11	27.68	26.80	40.33	27.68	26.72	28.62	27.79	
Ni	8.00	8.00	7.00	12.00	20.00	18.00	12.00	21.88	21.90	19.00	13.00	13.00	50.90	15.40	12.04	18.33	15.40	19.62	18.99	18.99	
Pb	15.50	18.00	20.00	14.00	22.00	21.00	25.00	15.08	19.60	20.00	26.00	21.00	17.59	22.00	19.00	18.00	22.00	21.00	17.87	16.49	
Pr	0.00	0.00	0.00	0.00	0.00	0.00	0.00	7.02	0.00	0.00	0.00	0.00	5.69	7.22	6.78	10.24	7.22	7.07	7.46	7.47	
Rb	127.50	72.00	138.00	92.00	78.00	159.00	133.00	64.59	118.05	125.00	130.00	106.00	106.04	143.34	129.81	155.43	143.34	151.29	159.15	150.40	
Sb	1.00	-3.00	-5.00	-6.00	-3.00	-4.00	3.00	-2.00	-3.00	-5.00	-4.00	-1.00	-4.50	-3.00	0.00	-3.00	0.00	0.00	-5.00	0.00	
Sc	16.50	12.00	11.00	12.00	18.00	14.00	11.00	15.50	17.00	13.00	10.00	12.00	14.06	12.80	11.64	17.51	12.80	13.89	16.44	15.29	
Se	0.00	-1.00	-1.00	0.00	-1.00	0.00	-1.00	0.00	0.00	-1.00	1.00	0.00	0.00	-1.00	0.00	-1.00	-1.00	0.00	0.00	-1.00	
Sm	7.50	-4.00	6.00	-2.00	7.00	0.00	-2.00	6.12	0.00	6.00	-3.00	-1.00	4.65	5.75	5.84	9.44	5.75	5.38	6.09	5.85	
Sn	2.00	2.00	2.00	3.00	0.00	3.00	4.00	3.00	-4.00	3.00	3.00	3.00	3.50	4.00	0.00	3.00	4.00	0.00	4.00	5.00	
Sr	204.50	137.00	148.00	223.00	208.00	129.00	124.00	180.77	148.55	158.00	121.00	111.00	127.01	161.14	124.96	171.46	161.14	162.01	206.50	199.39	
Ta	0.00	1.00	0.00	-1.00	-1.00	1.00	2.00	0.81	0.00	-1.00	1.00	-1.00	0.96	0.90	0.57	0.76	0.90	0.78	0.87	0.85	
Tb	0.00	0.00	0.00	0.00	0.00	0.00	0.00	0.86	0.00	0.00	0.00	0.00	0.58	0.64	0.94	1.59	0.64	0.57	0.69	0.70	
Th	11.50	8.00	12.00	8.00	11.00	12.00	13.00	12.19	9.35	12.00	13.00	12.00	10.89	11.69	11.94	14.82	11.69	11.16	10.81	9.98	
U	3.50	2.00	3.00	3.00	4.00	4.00	2.00	2.63	4.35	2.00	5.00	4.00	1.96	2.32	1.21	2.22	2.32	2.18	2.41	2.75	
V	130.00	81.00	111.00	99.00	136.00	121.00	103.00	103.63	128.30	112.00	103.00	91.00	90.74	84.75	61.28	92.75	84.75	93.39	101.07	97.09	
Y	32.00	23.00	29.00	28.00	38.00	29.00	22.00	26.87	31.60	28.00	23.00	23.00	18.49	12.32	34.30	53.97	12.32	10.87	16.35	19.15	
Yb	2.50	1.00	4.00	2.00	5.00	4.00	0.00	2.71	0.00	2.00	0.00	3.00	1.75	0.77	2.81	3.83	0.77	0.64	1.03	1.30	
Zn	90.50	63.00	94.00	79.00	90.00	76.00	78.00	100.30	87.50	86.00	77.00	63.00	98.92	88.94	63.88	96.64	88.94	97.03	94.39	93.22	
Zr	174.00	190.00	191.00	175.00	146.00	153.00	116.00	186.18	170.50	163.00	120.00	115.00	122.59	137.00	165.00	140.00	137.00	137.00	51.11	50.31	